

Behaviour of the Serre Equations in the Presence of Steep Gradients Revisited

Jordan Pitt,¹
Christopher Zoppou,¹
Stephen G. Roberts,¹

ABSTRACT

Keywords: dispersive waves, conservation laws, Serre equation, finite volume method, finite difference method

INTRODUCTION

The behaviour of steep gradients in a flow is important to shallow water modelling both because there are problems in which steep gradients are present in the initial conditions such as the propagation of a bore or the classical dam-break problem and also because some problems develop steep gradients as they evolve such as shoaling waves on a beach.

For our shallow water model of interest the Serre equations there are no analytic solutions to problems containing steep gradients. Although expressions have been derived for some important quantities such as the leading wave height and speed of an undular bore (El et al. 2006). Therefore to understand the more general structure of solutions to problems containing steep gradients we must turn to numerical methods to give us some insight.

Unfortunately there are few results which depict the behaviour of numerical solutions to the Serre equations in the presence of steep gradients (El et al. 2006; Le Métayer et al. 2010; Mitsotakis et al. 2016; Mitsotakis et al. 2014). These papers all present either travelling bores or the dam break problem and for two they present the same dam-break problem at different times (El et al. 2006; Le Métayer et al. 2010). There is however disagreement about the true nature of the solutions to these problems based on the presented numerical results.

Most of these papers have used some smoothing of the initial conditions to approximate the steep gradients present in the problem (El et al. 2006; Mitsotakis et al. 2016; Mitsotakis et al. 2014). There have also been comparisons for the dam-break problem between the analytic solutions of the shallow water wave equations and in some sense the mean behaviour of numerical results for the Serre equations (Le Métayer et al. 2010; Mitsotakis et al. 2014).

This paper makes use of a first, second and third-order numerical method (Zoppou et al. 2017) that is robust to steep gradients, with the first-order method being a recreation of the numerical method of Le Métayer et al. (2010). This paper also make use of two finite difference schemes, one is a recreation of the method of El et al. (2006) and the other is a naive finite difference approximation that makes for a good comparison.

These five different methods were then all used on the common dam-break problem (El et al. 2006; Le Métayer et al. 2010) to explain the disagreements in the nature of the solutions. It was found that the results of Le Métayer et al. (2010) were restricted by the diffusivity of the numerical

¹Mathematical Sciences Institute, Australian National University, Canberra, ACT 0200, Australia, E-mail: Jordan.Pitt@anu.edu.au. The work undertaken by the first author was supported financially by an Australian National University Scholarship.

method. While the results for the other papers were impacted by the smoothing of the initial conditions (El et al. 2006; Le Métayer et al. 2010). Through this process a new behaviour for our numerical results was found which has hitherto not been depicted. We also found that the analytic solutions for the shallow water wave equations are not precisely the mean behaviour of our solutions and our solutions disagree slightly with the Whitham modulation results of El et al. (2006).

The paper is organised as follows: The Serre equations are given as well as some important properties for validation, a reproducible expression of the two finite difference methods are given as well as the reformulation of the Serre equations into conservative form. Some numerical results are presented for the soliton problem to validate the finite difference methods and then the results of our numerical investigation into the behaviour of the Serre equations applied to the dam-break problem are presented.

SERRE EQUATIONS

The Serre equations can derived by integrating the full incompressible Euler equations over the water depth, see for example Su and Gardner (1969). They can also be derived as an asymptotic expansion of the Euler equations, see for example Lannes and Bonneton (2009). Assuming a constant horizontal bed the Serre equations are (Li et al. 2014)

$$\frac{\partial h}{\partial t} + \frac{\partial(uh)}{\partial x} = 0 \quad (1a)$$

and

$$\underbrace{\frac{\partial(uh)}{\partial t} + \frac{\partial}{\partial x} \left(u^2 h + \frac{gh^2}{2} \right)}_{\text{Shallow Water Wave Equations}} + \underbrace{\frac{\partial}{\partial x} \left(\frac{h^3}{3} \left[\frac{\partial u}{\partial x} \frac{\partial u}{\partial x} - u \frac{\partial^2 u}{\partial x^2} - \frac{\partial^2 u}{\partial x \partial t} \right] \right)}_{\text{Dispersion Terms}} = 0. \quad (1b)$$

Serre Equations

Where u is the average horizontal velocity over the depth of water h , g is the acceleration due to gravity, x is the horizontal spatial variable and t is time.

Conservation Laws

The Serre equations conserve mass (h), momentum (uh) and the Hamiltonian (\mathcal{H}) (Li 2002; Green and Naghdi 1976), thus our numerical methods should reflect this. The total amount of a quantity q in a system occurring on the interval $[a, b]$ is measured by

$$\mathcal{C}_q(t) = \int_a^b q(x, t) dx.$$

Conservation implies that $\mathcal{C}_h(0) = \mathcal{C}_h(t)$, $\mathcal{C}_{uh}(0) = \mathcal{C}_{uh}(t)$ and $\mathcal{C}_{\mathcal{H}}(0) = \mathcal{C}_{\mathcal{H}}(t) \forall t$ provided the interval is fixed and the system is closed.

The Hamiltonian is

$$\mathcal{H}(x, t) = \frac{1}{2} \left(hu^2 + \frac{h^3}{3} \left(\frac{\partial u}{\partial x} \right)^2 + gh^2 \right) \quad (2)$$

representing the energy in the system and is the sum of the kinetic energies in the horizontal (hu^2) and vertical ($\frac{h^3}{3} \left(\frac{\partial u}{\partial x} \right)^2$) directions and the gravitational potential energy (gh^2).

67 **DIRECT NUMERICAL METHODS FOR SOLVING THE SERRE EQUATIONS**

68 Zoppou et al. (2017) demonstrated that a numerical scheme for solving the Serre equations
 69 must be at least second-order accurate. The presence of the mixed spatial and temporal derivatives
 70 in the momentum equation (1b) makes the Serre equations difficult to solve with standard numeri-
 71 cal methods. The method of El et al. (2006) which we replicated used a second-order naive finite
 72 difference method to approximate (1b) which is both second-order and handles the mixed deriva-
 73 tive term. The continuity equation (1a) has no mixed derivative term allowing for the application of
 74 standard numerical techniques for conservation laws. In particular we have used a Lax-Wendroff
 75 method as in El et al. (2006) and for comparative purposes we also used a second-order naive finite
 76 difference method to approximate (1a). Together these two schemes make two methods for (1) the
 77 first being a recreation of the method of El et al. (2006) and the other being a naive second order
 78 finite difference approximation to (1). We begin with the common scheme, the second-order naive
 79 finite difference approximation to the momentum equation (1b).

80 **Finite Difference Approximation to Conservation of Momentum Equation**

81 To approximate all derivatives by finite differences requires that (1b) must be expanded, making
 82 use of (1a) one obtains

$$83 \quad h \frac{\partial u}{\partial t} + X - h^2 \frac{\partial^2 u}{\partial x \partial t} - \frac{h^3}{3} \frac{\partial^3 u}{\partial x^2 \partial t} = 0 \quad (3)$$

85 where

$$86 \quad X = uh \frac{\partial u}{\partial x} + gh \frac{\partial h}{\partial x} + h^2 \frac{\partial u}{\partial x} \frac{\partial u}{\partial x} + \frac{h^3}{3} \frac{\partial u}{\partial x} \frac{\partial^2 u}{\partial x^2} - h^2 u \frac{\partial^2 u}{\partial x^2} - \frac{h^3}{3} u \frac{\partial^3 u}{\partial x^3}$$

88 which contains only spatial derivatives. Taking the second-order centred finite difference approx-
 89 imation to (3) on a uniform grid in space such that $\Delta x = x_{i+1} - x_i \forall i$ and a uniform grid in time
 90 such that $\Delta t = t^{n+1} - t^n \forall n$ gives

$$91 \quad h_i^n u_i^{n+1} - (h_i^n)^2 \left(\frac{u_{i+1}^{n+1} - u_{i-1}^{n+1}}{2\Delta x} \right) - \frac{(h_i^n)^3}{3} \left(\frac{u_{i+1}^{n+1} - 2u_i^{n+1} + u_{i-1}^{n+1}}{\Delta x^2} \right) = -Y_i^n \quad (4)$$

93 and

$$94 \quad Y_i^n = 2\Delta t X_i^n - h_i^n u_i^{n-1} + (h_i^n)^2 \left(\frac{u_{i+1}^{n-1} - u_{i-1}^{n-1}}{2\Delta x} \right) + \frac{(h_i^n)^3}{3} \left(\frac{u_{i+1}^{n-1} - 2u_i^{n-1} + u_{i-1}^{n-1}}{\Delta x^2} \right)$$

96 where $q_i^n = q(x_i, t^n)$. Equation (4) can be rearranged into an explicit update scheme for u given
 97 its current and previous values, so that

$$98 \quad \begin{bmatrix} u_0^{n+1} \\ \vdots \\ u_m^{n+1} \end{bmatrix} = A^{-1} \begin{bmatrix} -Y_0^n \\ \vdots \\ -Y_m^n \end{bmatrix} =: \mathcal{G}_u(\mathbf{u}^n, \mathbf{h}^n, \mathbf{u}^{n-1}, \Delta x, \Delta t) \quad (5)$$

100 where A is a tri-diagonal matrix.

101 **The Lax-Wendroff Scheme for Conservation of Mass Equation**

102 The two step Lax-Wendroff update for h is

$$103 \quad h_{i+1/2}^{n+1/2} = \frac{1}{2} (h_{i+1}^n + h_i^n) - \frac{\Delta t}{2\Delta x} (u_{i+1}^n h_{i+1}^n - h_i^n u_i^n),$$

105

$$106 \quad h_{i-1/2}^{n+1/2} = \frac{1}{2} (h_i^n + h_{i-1}^n) - \frac{\Delta t}{2\Delta x} (u_i^n h_i^n - h_{i-1}^n u_{i-1}^n)$$

108 and

$$109 \quad h_i^{n+1} = h_i^n - \frac{\Delta t}{\Delta x} (u_{i+1/2}^{n+1/2} h_{i+1/2}^{n+1/2} - u_{i-1/2}^{n+1/2} h_{i-1/2}^{n+1/2}).$$

111 The quantities $u_{i\pm 1/2}^{n+1/2}$ are calculated using u^{n+1} obtained by applying \mathcal{G}_u from (5) to u^n then linearly
112 interpolating in space and time to give

$$113 \quad u_{i+1/2}^{n+1/2} = \frac{u_{i+1}^{n+1} + u_{i+1}^n + u_i^{n+1} + u_i^n}{4}$$

115 and

$$116 \quad u_{i-1/2}^{n+1/2} = \frac{u_i^{n+1} + u_i^n + u_{i-1}^{n+1} + u_{i-1}^n}{4}.$$

118 Thus we have the following update scheme for (1a)

$$119 \quad \mathbf{h}^{n+1} = \mathcal{E}_h (\mathbf{u}^n, \mathbf{h}^n, \mathbf{u}^{n+1}, \Delta x, \Delta t). \quad (6)$$

121 The update scheme combining (6) and (5) for all of (1) is therefore

$$122 \quad \left. \begin{aligned} \mathbf{u}^{n+1} &= \mathcal{G}_u (\mathbf{u}^n, \mathbf{h}^n, \mathbf{u}^{n-1}, \Delta x, \Delta t) \\ \mathbf{h}^{n+1} &= \mathcal{E}_h (\mathbf{u}^n, \mathbf{h}^n, \mathbf{u}^{n+1}, \Delta x, \Delta t) \end{aligned} \right\} \mathcal{E} (\mathbf{u}^n, \mathbf{h}^n, \mathbf{u}^{n-1}, \mathbf{h}^{n-1}, \Delta x, \Delta t). \quad (7)$$

124 **Second-Order Naive Finite Difference Method**

125 The mass equation (1a) is expanded then approximated by second-order centered finite differ-
126 ences after rearranging this to give an update formula we obtain

$$127 \quad h_i^{n+1} = h_i^{n-1} - \Delta t \left(u_i^n \frac{h_{i+1}^n - h_{i-1}^n}{\Delta x} + h_i^n \frac{u_{i+1}^n - u_{i-1}^n}{\Delta x} \right).$$

129 Preforming this update for all i will be denoted by $\mathcal{G}_h (\mathbf{u}^n, \mathbf{h}^n, \mathbf{h}^{n-1}, \Delta x, \Delta t)$. This update together
130 with (5) gives the naive second-order centred finite difference method for (1)

$$131 \quad \left. \begin{aligned} \mathbf{h}^{n+1} &= \mathcal{G}_h (\mathbf{u}^n, \mathbf{h}^n, \mathbf{h}^{n-1}, \Delta x, \Delta t) \\ \mathbf{u}^{n+1} &= \mathcal{G}_u (\mathbf{u}^n, \mathbf{h}^n, \mathbf{u}^{n-1}, \Delta x, \Delta t) \end{aligned} \right\} \mathcal{G} (\mathbf{u}^n, \mathbf{h}^n, \mathbf{u}^{n-1}, \mathbf{h}^{n-1}, \Delta x, \Delta t). \quad (8)$$

133

134 **CONSERVATIVE FORM OF THE SERRE EQUATIONS**

135 To overcome the aforementioned difficulty of mixed derivatives, (1) can be reformulated into
 136 conservative form. This was accomplished by the introduction of a new quantity (Le Métayer et al.
 137 2010; Zoppou et al. 2017)

138
$$G = uh - h^2 \frac{\partial h}{\partial x} \frac{\partial u}{\partial x} - \frac{h^3}{3} \frac{\partial^2 u}{\partial x^2}. \quad (9)$$

 139

140 Consequently, (1) can be rewritten as

141
$$\frac{\partial h}{\partial t} + \frac{\partial(uh)}{\partial x} = 0 \quad (10a)$$

 142

143 and

144
$$\frac{\partial G}{\partial t} + \frac{\partial}{\partial x} \left(Gu + \frac{gh^2}{2} - \frac{2h^3}{3} \frac{\partial u}{\partial x} \frac{\partial u}{\partial x} \right) = 0. \quad (10b)$$

 145

146

147 **A Hybrid Finite Difference-Volume Method for Serre Equations in Conservative Form**

148 The conservative form (10) allows for a wider range of numerical techniques such as finite
 149 element methods (Li et al. 2014) and hybrid finite difference-volume hybrid methods (Le Métayer
 150 et al. 2010; Zoppou 2014). In this paper the first (\mathcal{V}_1), second (\mathcal{V}_2) and third-order (\mathcal{V}_3) hybrid finite
 151 difference-volume methods of Zoppou et al. (2017) will be used. Instead of solving (1) directly
 152 these hybrid finite difference-volume methods solve the equivalent formulation (10) with a finite
 153 volume method for the conserved variables h and G with the the remaining primitive variable u
 154 reconstructed from a finite difference approximation of (9). These methods all introduce diffusive
 155 errors, were found to have the appropriate order of accuracy and were tested agaisnt experimental
 156 data involving steep gradients.

157 **Stability Condition**

To ensure stability of the hybrid finite difference-volume methods the time-step Δt must satisfy the Courant-Friedrichs-Lewy (CFL) criteria (A. Harten 1983)

$$\Delta t < \frac{Cr\Delta x}{2 \max \{|\lambda|\}} \quad (11)$$

158 with $0 < Cr \leq 1$ where λ is the charachteristic speed. For the Serre equations it has been
 159 demonstrated that the wave speed is bounded by the charachteristic speed of the shallow water
 160 wave equations (Le Métayer et al. 2010; Zoppou et al. 2017).

161 Performing a Von-Neumann stability analysis for \mathcal{G} (8) and \mathcal{E} (7) applied to the linearised Serre
 162 equations (Zoppou et al. 2017) it was found that the CFL condition (11) ensures stability for \mathcal{G} .
 163 It was also found that \mathcal{E} was stable with this CFL condition when there was no background flow.
 164 With some background flow \mathcal{E} is unconditionally unstable although we observed growth factors
 165 marginally above 1 for the flow regimes in this paper using the CFL condition, with smaller time-
 166 steps allowing for smaller growth factors.

167 **NUMERICAL SIMULATIONS**

168 In this section the methods introduced in this paper will be validated by using them to approx-
169 imate an analytic solution of the Serre equations, this will also be used to verify their order of
170 accuracy. This will be followed by an in-depth comparison of these methods for a smooth approx-
171 imation to the discontinuous dam-break problem to investigate the behaviour of these numerical
172 schemes and therefore the Serre equations in the presence of steep gradients.

173 **SOLITARY WAVES**

174 Cnoidal waves propagate without deformation and are the only family of analytic solutions
175 to the Serre equations (Carter and Cienfuegos 2011). Solitary waves are a particular instance of
176 cnoidal waves which have been used to verify the convergence rates of the described methods in
177 this paper.

178 The solitary waves of the Serre equations have the following form

179
$$h(x, t) = h_0 + A \operatorname{sech}^2(\kappa(x - ct)), \quad (12a)$$

180

182
$$u(x, t) = c \left(1 - \frac{h_0}{h(x, t)}\right), \quad (12b)$$

183

185
$$\kappa = \frac{\sqrt{3A}}{2h_0\sqrt{h_0 + A}} \quad (12c)$$

186 and

188
$$c = \sqrt{g(h_0 + A)} \quad (12d)$$

190 where h_0 and A determine the depth of the quiescent water and the peak amplitude of the soli-
191 tary wave respectively. In these simulations $h_0 = 1\text{m}$, $A = 0.7\text{m}$ for $x \in [-50\text{m}, 250\text{m}]$ and
192 $t \in [0\text{s}, 50\text{s}]$. With $\Delta t = 0.5\lambda^{-1}\Delta x$ where $\lambda = \sqrt{g(h_0 + A)}$ which is the maximum wave
193 speed, this satisfies the CFL condition (11) and makes the results comparable to those presented
194 by Zoppou et al. (2017) for the finite difference-volume hybrid methods. Since this problem has no
195 background flow this means that both \mathcal{G} and \mathcal{E} are stable throughout these numerical simulations
196 using this value of λ .

197 **Results**

198 From Figure 1 it can be seen that the numerical methods \mathcal{G} (8) and \mathcal{E} (7) accurately model the
199 highly non-linear solitary wave problem, reproducing the analytic solution at $t = 50\text{s}$.

To demonstrate that in fact \mathcal{E} and \mathcal{G} properly capture the behaviour of the Serre equations, two measures were used. The first measures the relative distance of the numerical results from the analytic solution for h and u , it is defined for a general quantity q and an approximation to it q^* at n spatial nodes as

$$L_1 = \frac{\sum_{i=1}^n |q_i - q_i^*|}{\sum_{i=1}^n |q_i|}.$$

The second measures how well a scheme conserves a quantity q over time

$$C_1 = \frac{|\mathcal{C}_q(0) - \mathcal{C}_{q^*}(t_f)|}{|\mathcal{C}_q(0)|}$$

where t_f is the final time of the numerical experiment. For $\mathcal{C}_q(0)$ the analytic value is used while a numerical calculation is used for $\mathcal{C}_{q^*}(t_f)$ based on summing cell-wise integrals. For consistency all cell-wise integrals are calculated by quartic interpolation of h and u utilising neighbouring cells and then applying Gaussian quadrature with 3 points over the cell to get a sufficiently high order approximation so that only the errors of the numerical scheme for the Serre equations are dominant.

From Figure 2 it can be seen that both finite difference methods are convergent under L_1 with second-order accuracy. There is however suboptimal rates of convergence for very small Δx due to round off effects and suboptimal rates of convergence for large Δx due to the initial conditions not being accurately represented on a coarse grid. Figure 2 demonstrates conservation of mass, momentum and the Hamiltonian to at least second-order accuracy for both finite difference schemes. Both schemes conserve mass and momentum very well with round off error dominance occurring at the same place as for L_1 . For C_1 of \mathcal{H} the effects of round off errors occur earlier due to the greater number of calculations.

All of these measures demonstrate that \mathcal{G} and \mathcal{E} are appropriate to solve highly non-linear problems with smooth initial conditions for the Serre equations.

SMOOTHED DAM-BREAK

The discontinuous dam-break problem can be approximated smoothly using the hyperbolic tangent function. Such an approximation will be called a smoothed dam-break problem and will be defined as such

$$h(x, 0) = h_0 + \frac{h_1 - h_0}{2} \left(1 + \tanh \left(\frac{x_0 - x}{\alpha} \right) \right), \quad (13a)$$

$$u(x, 0) = 0.0m/s. \quad (13b)$$

Where α measures the distance over which 46.117% of the smooth transition between the two heights of h_0 and h_1 centered around x_0 occurs. Figure 3 demonstrates the effect of varying α for the smoothed dam-break problem with $h_1 = 1.8m$, $h_0 = 1m$ and $x_0 = 500m$. These are the same h_0 and h_1 values as those of the dam-breaks presented by El et al. (2006) and Le Métayer et al. (2010) and will be the values used throughout this paper.

From (13) the following expressions for $\mathcal{C}_h(0)$, $\mathcal{C}_{uh}(0)$ and $\mathcal{C}_{\mathcal{H}}(0)$ were derived provided x_0 is the midpoint of the spatial domain $[a, b]$ in which the smoothed dam-break occurs

$$\mathcal{C}_h(0) = \frac{h_1 + h_0}{2} (b - a),$$

$$\mathcal{C}_{uh}(0) = 0$$

237 and

238

$$\mathcal{C}_H(0) = \frac{g}{4} \left(h_0^2 - h_1^2 + \alpha (h_1 - h_0)^2 \tanh \left(\frac{a-b}{2\alpha} \right) \right).$$

239

240 Note that due to a difference in heights at the two boundaries there is a flux of momentum into the
241 system equal to $t g(h^2(b) - h^2(a))$ and this must be accounted for in C_1 of uh .

242 The dam-break problem for the Serre equations results in the creation of an undular bore that is
243 very similar to the analytic solution of the dam-break problem for the shallow water wave equations
244 with oscillations (Le Métayer et al. 2010; Mitsotakis et al. 2014). Because the analytic solution
245 to the dam-break problem for the shallow water wave equations will be used as a reference in this
246 paper we present it in Figure 4 for $h_0 = 1m$, $h_1 = 1.8m$ and $x_0 = 500m$ at $t = 30s$. The regions
247 I through V in Figure 4 will be used to simplify our explanations later on for numerical solutions
248 of the Serre equations. We also present equations for the quantities of interest in the analytic
249 solution of the dam-break problem for the shallow water wave equations; the constant height (h_2)
250 and velocity (u_2) in regions III and IV and the speed of the shock (S_2) which marks the boundary
251 between regions IV and V. From Wu et al. (1999) we have the following equations

252

$$h_2 = \frac{h_0}{2} \left[\sqrt{1 + 8 \left(\frac{2h_2}{h_2 - h_0} \frac{\sqrt{gh_1} - \sqrt{gh_2}}{\sqrt{gh_0}} \right)^2} - 1 \right], \quad (15a)$$

253

254

$$u_2 = 2 \left(\sqrt{gh_1} - \sqrt{gh_2} \right) \quad (15b)$$

255

256 and

257

$$S_2 = \frac{h_2 u_2}{h_2 - h_0}. \quad (15c)$$

258

259 From these values we also define $x_{u_2}(t) = x_0 + u_2 t$ and $x_{S_2}(t) = x_0 + S_2 t$ to give the location of
260 a fluid particle starting at x_0 travelling at speed u_2 and S_2 respectively at time t .

261 Undular bores for the one dimensional Serre equations were analysed by El et al. (2006) and an
262 expression for the amplitude (A^+) and speed (S^+) of the leading wave of a bore shown in Figure 5
263 were given

264

$$\frac{\Delta}{(A^+ + 1)^{1/4}} - \left(\frac{3}{4 - \sqrt{A^+ + 1}} \right)^{21/10} \left(\frac{2}{1 + \sqrt{A^+ + 1}} \right)^{2/5} = 0 \quad (16a)$$

265

266

$$S^+ = \sqrt{g(A^+ + 1)} \quad (16b)$$

267

268 where $\Delta = h_b/h_0$, and h_b is the amplitude of the bore. From this we define $x_{S^+}(t) = x_0 + S^+ t$
269 which is the location of a fluid particle starting at x_0 and travelling at speed S^+ at time t .

270 The simulations were run with various values of Δx and α . In regions III and IV there is a
271 background flow and so \mathcal{E} is unstable, to account for this the growth factor was suppressed by
272 using a smaller time step than the CFL condition of $\Delta t = 0.01\Delta x$. \mathcal{V}_2 requires an input parameter
273

²⁷⁴ to its slope limiter and this was chosen to be $\theta = 1.2$ (Zoppou et al. 2017). The first set of scenarios
²⁷⁵ presented were run until $t = 30s$ on the interval $x \in [0m, 1000m]$.

Applying (15) to our dam-break problem results in $h_2 = 1.36898m$, $u_2 = 1.074975 m/s$ and $S_2 = 3.98835 m/s$ which can be seen in Figure 4. For (16) as in El et al. (2006) the height of the bore is given as

$$h_b = \frac{\left(\sqrt{\frac{h_1}{h_0}} + 1\right)^2}{4}.$$

²⁷⁶ Thus $h_b = 1.37082 m$, $\Delta = 1.37082$, $A^+ = 1.73998 m$ and $S^+ = 4.13148 m/s$. Note that due to
²⁷⁷ the different natures of bores for the Serre and shallow water wave equations $S^+ \neq S_2$.

²⁷⁸ Results

²⁷⁹ We begin this study by looking into the effect of the initial steepness of the smoothed dam-break
²⁸⁰ problem for different α values by observing what happens as $\Delta x \rightarrow 0$ and our numerical solution
²⁸¹ better approximates the true solution of the Serre equations. To have the smallest error we use the
²⁸² highest order well validated model \mathcal{V}_3 in the following investigation. From these results we then
²⁸³ investigate numerical results for long time scales, how the shallow water wave equations analytic
²⁸⁴ solution and El's Whitham modulation values compare to our results and then finally present some
²⁸⁵ other findings about the behaviour of our numerical solutions.

²⁸⁶ Effect of α

²⁸⁷ Because the smoothing process is a non-physical numerical tool we first study its effect by de-
²⁸⁸ creasing α and thus better approximating the dam-break. To do this we fix an α and then investigate
²⁸⁹ the numerical solutions as $\Delta x \rightarrow 0$ and our well validated numerical method better approximates
²⁹⁰ the true solution of the Serre equations.

²⁹¹ The first observation is that there are four types of behaviour as $\Delta x \rightarrow 0$ depending on the
²⁹² α and the numerical method. The four behaviours are identified by the nature of the solutions
²⁹³ around x_{u_2} when Δx is small and they correspond to different results presented in the literature.
²⁹⁴ For brevity the only given examples of these behaviours will be the solutions of \mathcal{V}_3 although they
²⁹⁵ all also occurred for the \mathcal{E} , \mathcal{G} and \mathcal{V}_2 simulations using the same α and $\Delta x = 10/2^{10}m$.

²⁹⁶ The first behaviour which will be referred to as the non-oscillatory behaviour has such smooth
²⁹⁷ initial conditions that no oscillations were introduced by $t = 30s$ for the numerical simulations,
²⁹⁸ although given sufficient time the front steepens and an undular bore will develop. This behaviour
²⁹⁹ is not present in the literature as no authors chose large enough α values. An example of this
³⁰⁰ behaviour can be seen in Figure 6 for $\alpha = 40m$. Because this is a very smooth problem we
³⁰¹ observe that all numerical results are visually identical for all $\Delta x < 10/2^4m$. We observed this
³⁰² behaviour for \mathcal{V}_1 's simulations as well. We note that \mathcal{V}_3 's numerical solution has $h(x_{u_2}) > h_2$ and
³⁰³ because no undulations are present El et al. (2006) results are not applicable to these solutions.

³⁰⁴ Convergence is also present in Figure 7 with both the L_1 and C_1 measures. Here L_1 has been
³⁰⁵ modified to use the numerical solution when $\Delta x = 10/2^{10}m$ as an approximation to the analytic
³⁰⁶ solution because none are currently known for the Serre equations. For L_1 and C_1 of \mathcal{H} the order
³⁰⁷ of accuracy is the theoretical one. Since L_1 compares only numerical results, round-off errors
³⁰⁸ result in error stagnation rather than increase as in Figure 2. C_1 for h demonstrates that the finite
³⁰⁹ volume method does indeed conserve mass independent of Δx with round-off errors dominant for
³¹⁰ all tested Δx . C_1 of uh has been omitted because there is a small but noticeable flux of momentum

311 at the boundaries due to the large α , which dominates the errors and cannot be accounted for.
312 The presented measures suggest that this family of solutions is an accurate representation of the
313 behaviour of the Serre equations when α is sufficiently large and in particular $\alpha = 40m$.

314 The second behaviour will be referred to as the flat behaviour due to the presence of a constant
315 height around x_{u_2} , this is the most common behaviour observed in the literature (Le Métayer et al.
316 2010; Mitsotakis et al. 2014; Mitsotakis et al. 2016). This behaviour has oscillations in regions III
317 and IV which are separated by a constant height state around x_{u_2} . An example of the numerical
318 results for this behaviour can be seen in Figure 8 when $\alpha = 2m$.

319 As Δx decreases the solutions converge so that by $\Delta x = 10/2^8 m$ the solutions for higher Δx
320 are visually identical. There is also good agreement between the peak amplitude in region IV (A)
321 and A^+ as well as $h(x_{u_2})$ and h_2 . Although as Δx is decreased in the simulations we observe
322 $h(x_{u_2}) > h_2$. Since this method is well validated for smooth problems and a small Δx has been
323 chosen this suggests that the mean bore heights in regions III and IV from a dam-break may differ
324 slightly between the shallow water wave equations and the Serre equations. These results also
325 compare well to the results in Mitsotakis et al. (2016) who use the same α but different h_0 and h_1 .
326 We observed this behaviour for \mathcal{V}_1 's simulations.

327 The measures L_1 and C_1 demonstrate good convergence with the expected order of accuracy.
328 For \mathcal{V}_3 we observe that C_1 of uh has a larger error but a higher order of accuracy than C_1 of \mathcal{H} .
329 The higher order of accuracy makes sense as the conversion between the conserved quantity G
330 and u is fourth order. The smaller C_1 error of \mathcal{H} can be explained by noting that although uh is a
331 component of \mathcal{H} , gh^2 makes up a far larger portion of \mathcal{H} see Figure 21, diminishing the relative
332 size of the uh errors in \mathcal{H} .

333 These results demonstrate that this behaviour is an accurate representation of the nature of the
334 Serre equations provided α is large enough supporting the findings of Mitsotakis et al. (2016).

335 The third behaviour will be referred to as the node behaviour and it was observed by El et al.
336 (2006). The node behaviour's main feature is that the oscillations in region III and IV decay and
337 appear to meet at x_{u_2} as can be seen in Figure 10 when $\alpha = 0.4m$. All the methods have not
338 converged to a solution as Δx decreases. However, it does appear that convergence is likely with
339 the solutions getting closer together. This is expected for the smaller Δx because the problem is
340 still smooth. In these results A^+ is a good estimator for A and the oscillations in regions III and
341 IV appear to be around h_2 . This behaviour was observed by El et al. (2006) for \mathcal{E} and indeed
342 we have replicated it for all the high order methods. It was not observed in \mathcal{V}_1 's solutions up
343 to $\Delta x = 10/2^{10} m$ with $\alpha = 0.001m$ as \mathcal{V}_1 introduces diffusive errors that severely dampen the
344 oscillations. This explains why Le Métayer et al. (2010) using \mathcal{V}_1 could not replicate the results of
345 El et al. (2006). It was found that an α of at least $0.4m$ is required to recover the node behaviour
346 this explains why Mitsotakis et al. (2016) and Mitsotakis et al. (2014) using α 's of $2m$ and $1m$
347 respectively could not replicate the results of El et al. (2006).

348 The assertion that these results are close to converging to a solution is supported by Figure 11
349 with appropriate orders of accuracy for L_1^* and C_1 . Figure 10 demonstrates that the final solutions
350 have not yet converged, thus we modify L_1 to omit $[520m, 540m]$ and call this modified measure
351 L_1^* . L_1^* demonstrates that even though the section around x_{u_2} has not been fully resolved we do see
352 that there is convergence at the appropriate order away from x_{u_2} . This suggests that the effect of
353 better resolving the oscillations will only be felt locally. C_1 demonstrates the appropriate order of
354 accuracy in conserving momentum and the Hamiltonian suggesting that we are indeed approaching
355 a reasonable solution to this problem as Δx is decreased.

356 These results demonstrate that although we have not yet fully converged this behaviour is close
357 to reasonable solutions of the Serre equations given the appropriate α value supporting the findings
358 of El et al. (2006).

359 The fourth behaviour will be referred to as the bump behaviour due to the oscillations no longer
360 decaying down towards a point but rather growing around x_{u_2} forming a bump as can be seen in
361 Figure 12 for $\alpha = 0.1m$. This behaviour has hitherto not been published and is certainly not an
362 expected result.

363 This behaviour is even further from converging with decreasing Δx around x_{u_2} than the node
364 behaviour as can be seen in Figure 12. L_1^* demonstrates good convergence outside this middle
365 region as can be seen in Figure 13 so that resolving the region around x_{u_2} is the main difficulty
366 for our numerical methods. C_1 of uh and \mathcal{H} also converges but compared to the other behaviours
367 we have lost an order of accuracy in these measures. This suggests that we are not using the
368 appropriate Δx and thus smaller grids are required to attain the appropriate order of convergence
369 for \mathcal{V}_3 . Because, convergence is not assured by these numerical results there is the possibility that
370 the wave amplitudes around the x_{u_2} could grow rapidly. This however has not been observed, with
371 numerical results where $\alpha = 0.001m$ and $\Delta x = 10.0/2^{10}m$ at which point the initial conditions are
372 basically a discontinuous dam-break showing an increase but not a large growth in the amplitude
373 of the bump for \mathcal{V}_3 .

374 Since this result is unexpected and not as supported as the node behaviour in the literature (El
375 et al. 2006). The first check should be different numerical methods such as \mathcal{G} and \mathcal{E} to test if
376 some numerical effect from the reformulation of the Serre equations or the elliptic solver are the
377 cause. For comparison \mathcal{G} , \mathcal{E} , \mathcal{V}_1 and \mathcal{V}_3 are applied to the same initial conditions with the same
378 grid resolutions as above and the results were plotted in Figure 14. \mathcal{V}_2 has been omitted from this
379 figure for clarity because its solution is very close to \mathcal{V}_3 as noted by Zoppou et al. (2017). The
380 first observation is that \mathcal{V}_1 has not recovered this behaviour. This is because \mathcal{V}_1 is very diffusive
381 (Zoppou et al. 2017), dampening these oscillations. To resolve such behaviour for \mathcal{V}_1 would require
382 very small Δx and as such this has not been observed in the simulations. Secondly, all high-
383 order methods recover this bump behaviour and disagree only in the region around x_{u_2} . The
384 main difference in the oscillations is their phase and amplitude with the dispersive finite difference
385 methods resulting in larger waves than the diffusive finite difference-volume hybrid methods. We
386 also observe oscillations in \mathcal{E} that are not replicated by the other methods close to x_{u_2} , this is
387 caused by the instability of \mathcal{E} with its effects being more obvious here due to the high frequency of
388 these waves which correspond to larger growth factors.

389 Since \mathcal{V}_3 is diffusive as can be seen in Figure 12 and \mathcal{G} is dispersive the true analytic solution
390 should exist between \mathcal{V}_3 and \mathcal{G} , which is a bounded bump around x_{u_2} . \mathcal{G} well approximates the
391 Serre equations, although \mathcal{V}_2 and \mathcal{V}_3 are still preferred by the authors due to their robustness and
392 superior conservation of quantities.

393 There is still the possibility that these solutions are caused by some numerical phenomena,
394 more research into this topic should be undertaken. However, the agreement of all the discussed
395 methods of sufficiently high order indicates that these results are representative of actual solutions
396 of the smoothed dam-break problem with low α for the Serre equations. Lastly the bump behaviour
397 was observed using \mathcal{E} with a similar order of magnitude for Δx and Δt as El et al. (2006). The
398 absence of a bump behaviour in their findings is caused by the smoothing of the initial conditions
399 which is absent from the paper but was confirmed later by El and Hoefer (2016).

400 This concludes the explanation of how our results fit in with the current literature and the

401 following section of this paper will be concerned with some further numerical investigation into
402 these results.

403 *Long time*

404 The first test of these results will be of its evolution through time, thus an experiment was run
405 with the same parameters on a larger domain with $x \in [-900m, 1800m]$ for $t \in [0, 300s]$. The
406 results of \mathcal{V}_3 with $\alpha = 0.1m$ and $\Delta x = 10/2^9 m$ and $10/2^8 m$ at $t = 300s$ are presented in Figure
407 15. For this problem these parameters result in the bump behaviour as can be seen in Figure 12,
408 however after sufficient time we can see that this bump behaviour has decayed back into a flat
409 behaviour although there are still small oscillations present in the middle region.

410 We also observe that A^+ has not been perfectly replicated with the numerical solution having
411 larger peak amplitudes in region IV than A^+ . Consequently we can see that while x_{S+} is a better
412 approximation than x_{S_2} to the position of the bore it is still an underestimate. Thus our bores will
413 arrive a little earlier than predicted by S^+ and much earlier than predicted by S_2 . We also note
414 that as above the bore heights for the Serre and shallow water wave equations appear to be slightly
415 different.

416 To track the decaying of the oscillations for \mathcal{V}_3 's solution around x_{u_2} a snapshot of the area
417 around x_{u_2} has been plotted for different times in Figure 16. It can be seen that at $t = 30s$ the
418 solution exhibits the bump behaviour but as time progresses the region around x_{u_2} has decayed
419 into the node behaviour by $t = 100s$ and then into the flat behaviour observed at $t = 200s$ and
420 $t = 300s$. This could be a property of the solution of the Serre equations after sufficient time or due
421 to the accumulation of diffusive errors of the numerical method with Figure 15 demonstrating that
422 over this time span we are not close to convergence of the numerical results. We note that El et al.
423 (2006) had very similar results in this longer time scale although their paper uses the normalised
424 Serre equations so that in effect $g = 1m/s^2$ and an unknown smoothing of the initial conditions
425 which make comparisons of the solutions at similar times difficult.

426 *Shallow water wave equation comparison*

427 Since the shallow water wave equations have been used as a guide for the mean behaviour
428 of the solution of the Serre equations in the literature (Le Métayer et al. 2010; Mitsotakis et al.
429 2016) we would like to investigate how useful they are. We first plot $h - h_2$ and $u - u_2$ for the
430 smoothed dam-break problem with $\alpha = 0.1m$ and $\Delta x = 10/2^9 m$ in Figure 17 for $t = 30s$ and
431 Figure 18 for $t = 300s$. From this we can see that over short time spans both h_2 and u_2 are good
432 approximations to the mean behaviour of the fluid with both plots oscillating around 0. However
433 after sufficient time we see that the mean velocity and height of the fluid have diverged slightly
434 from the shallow water wave equation values h_2 and u_2 . With h_2 being an underestimate and u_2
435 being an overestimate. From Figure 15 it can also be seen that S_2 underestimates the speed of the
436 bore front.

437 From Figure 17 and Figure 18 it can be seen that to the left of x_{u_2} u and h are anti-phase
438 while to the right of x_{u_2} u and h are in-phase. The contact discontinuity (El et al. 2006) marks the
439 transition between these two states which is located at about x_{u_2} . Figure 18 demonstrates that at
440 x_{u_2} , h and u are in-phase therefore the contact discontinuity is to the left of x_{u_2} , thus the speed of
441 the contact discontinuity like the mean bore velocity is slightly overestimated by u_2 .

442 Because h and u are anti-phase to the left of the contact discontinuity they appear to travel
443 leftwards relative to it while those on the right are in-phase and therefore appear to travel rightwards
444 relative to the contact discontinuity. Thus these oscillations appear to be forming at the contact

discontinuity and then travelling away from it. The phase velocity of the linearised Serre equations is

$$v_p = u \pm \sqrt{gh} \sqrt{\frac{3}{h^2 k^2 + 3}}$$

where k is the wave number. The phase velocity has the following behaviour, as $k \rightarrow \infty$ then $v_p \rightarrow u$ and as $k \rightarrow 0$ then $v_p \rightarrow u \pm \sqrt{gh}$. Since we observe u and h as being anti-phase to the left of the contact discontinuity this means we are in the negative branch of the phase velocity $u - \sqrt{gh} \sqrt{\frac{3}{h^2 k^2 + 3}}$ while the in-phase right side corresponds to the positive branch $u + \sqrt{gh} \sqrt{\frac{3}{h^2 k^2 + 3}}$. Thus the contact discontinuity corresponds to oscillations with very high wave numbers, which are sensitive to both smoothing of the initial conditions and numerical diffusion. By this phase velocity argument the contact discontinuity should travel at the mean bore velocity which is close to u_2 for a range of dam-break problems. To investigate this $h_0 = 1m$ was fixed and h_1 was varied to allow for different aspect ratios and thus different bore speeds. The results are plotted in Figure 19 from which it is quite clear that the contact discontinuity does in fact travel at close to u_2 for a range of aspect ratios.

Whitham modulation comparison

The expressions for the leading wave amplitude A^+ and speed S^+ obtained by El et al. (2006) are asymptotic results and so we are interested in how our numerical results behave over time. Thus for the dam-break problem in Figure 15 the peak amplitude in region IV (A) was plotted over time in Figure 20. From the figure it can see that A approaches a value larger than A^+ . We find that as $\alpha \rightarrow 0$ and $\Delta x \rightarrow 0$ our A values converge away from A^+ not towards it in this time scale for this aspect ratio. Thus it appears that the true solution of the dam-break for the Serre equations has an amplitude in region IV slightly above A^+ . This is not inconsistent with the results of (El et al. 2006) as their scale comparing A^+ to numerical solutions is too large to see such a small difference. From Figure 15 it can be seen that while S^+ does not precisely predict the bore speed it is a better prediction than S_2 .

Energy Breakdown

The Hamiltonian (2) has 3 terms representing in order, horizontal kinetic energy hu^2 , vertical kinetic energy $\frac{h^3}{3} \frac{\partial u}{\partial x}$ and gravitational potential energy gh^2 . It might be expected that the oscillations of the undular bore such as in Figure 15 would result in significant vertical energies. However, Figure 21 demonstrates that this is not the case, as the total vertical kinetic energy in the system is insignificant relative to the other energies. This plot also demonstrates that even with dispersive terms and large oscillations the drivers of change in the dam-break problem are the transfer of gravitational potential energy into horizontal kinetic energy which occurs slowly.

CONCLUSIONS

Utilising two finite difference methods of second-order and three finite difference-volume hybrid methods of various orders an investigation into the smoothed dam-break problem with varying steepness was performed. Four different behaviours were uncovered with the general trend being that an increase in steepness increases the size and number of oscillations in the solution. This study explains all current differences in the literature involving the solution of the Serre equations applied to the smoothed dam-break problem and also uncovers a new result. We find that while the analytic solution of the shallow water wave equations for the dam-break problem is a good guide to

485 the mean behaviour of the Serre equations the speed and height of the bores do not match up pre-
486 cisely. While the Whitham modulation results for the Serre equations give better predictions than
487 the shallow water wave equations analytic solution it was found that they also do not line up with
488 our numerical results precisely. It was demonstrated that the contact discontinuity corresponds to
489 high wave numbers and thus travels at the mean velocity inside the bore. It was also found that
490 vertical kinetic energy is negligible for the dam-break problem.

491 REFERENCES

- 492 A. Harten, A. (1983). "High resolution schemes for hyperbolic conservation laws." *Journal of*
493 *Computational Physics*, 49(3), 357–393.
- 494 Carter, J. D. and Cienfuegos, R. (2011). "Solitary and cnoidal wave solutions of the Serre equations
495 and their stability." *European Journal of Mechanics B/Fluids*, 30(3), 259–268.
- 496 El, G., Grimshaw, R. H. J., and Smyth, N. F. (2006). "Unsteady undular bores in fully nonlinear
497 shallow-water theory." *Physics of Fluids*, 18(027104).
- 498 El, G. and Hoefer, M. (2016). "Dispersive shock waves and modulation theory." *Physica D: Non-*
499 *linear Phenomena*, 333, 11–65.
- 500 Green, A. E. and Naghdi, P. M. (1976). "A derivation of equations for wave propagation in water
501 of variable depth." *Journal of Fluid Mechanics*, 78(2), 237–246.
- 502 Lannes, D. and Bonneton, P. (2009)." *Physics of Fluids*, 21(1), 16601–16610.
- 503 Le Métayer, O., Gavrilyuk, S., and Hank, S. (2010). "A numerical scheme for the GreenNaghdi
504 model." *Journal of Computational Physics*, 229(6), 2034–2045.
- 505 Li, M., Guyenne, P., Li, F., and Xu, L. (2014). "High order well-balanced CDG-FE methods for
506 shallow water waves by a Green-Naghdi model." *Journal of Computational Physics*, 257, 169–
507 192.
- 508 Li, Y. A. (2002). "Hamiltonian Structure and Linear Stability of Solitary Waves of the Green-
509 Naghdi Equations." *Journal of Nonlinear Mathematical Physics*, 9, 99–105.
- 510 Mitsotakis, D., Dutykh, D., and Carter, J. (2016). "On the nonlinear dynamics of the traveling-wave
511 solutions of the serre system." *Wave Motion*.
- 512 Mitsotakis, D., Ilan, B., and Dutykh, D. (2014). "On the Galerkin/Finite-Element Method for the
513 Serre Equations." *Journal of Scientific Computing*, 61(1), 166–195.
- 514 Su, C. H. and Gardner, C. S. (1969). "Korteweg-de Vries equation and generalisations. III. Deriva-
515 tion of the Korteweg-de Vries equation and Burgers equation." *Journal of Mathematical Physics*,
516 10(3), 536–539.
- 517 Wu, C., Huang, G., and Zheng, Y. (1999). "Theoretical solution of dam-break shock wave." *Journal*
518 *of Hydraulic Engineering*, 125(11), 1210–1215.
- 519 Zoppou, C. (2014). "Numerical solution of the One-dimensional and Cylindrical Serre Equations
520 for Rapidly Varying Free Surface Flows." Ph.D. thesis, Australian National University, Mathe-
521 matical Sciences Institute, College of Physical and Mathematical Sciences, Australian National
522 University, Canberra, ACT 2600, Australia.
- 523 Zoppou, C., Pitt, J., and Roberts, S. (2017). "Numerical solution of the fully non-linear weakly
524 dispersive serre equations for steep gradient flows." *Applied Mathematical Modelling*, 00(00),
525 00–00.

526 **List of Figures**

527 1	Comparison between water profile of analytic solution (—) of the solitary wave problem (12) and numerical solution (●) with $\Delta x = 10/2^{12}m$ for \mathcal{G} (a) and \mathcal{E} (b) at $t = 50s$	17
530 2	On the left L_1 for h (\triangle) and u (\square) and on the right C_1 for h (\triangle), uh (\diamond) and \mathcal{H} (\circ) for the numerical solution of the solitary wave problem by \mathcal{G} (a) and \mathcal{E} (b).	18
532 3	Initial conditions for the smooth dam-break problem with $h_0 = 1m$, $h_1 = 1.8m$ and $x_0 = 500m$ as α varies.	19
534 4	Analytic solution at $t = 30s$ of the shallow water wave equations for the dam-break problem with $h_0 = 1m$, $h_1 = 1.8m$ and $x_0 = 100m$	20
536 5	Demonstration of quantities obtained by Whitham modulation for undular bores of the Serre equations.	21
538 6	Numerical results of \mathcal{V}_3 at $t = 30s$ for the smooth dam-break problem with $\alpha = 40m$ for $\Delta x = 10/2^4m$ (—).	22
540 7	On the left is L_1 for h (\triangle) and u (\square) and on the right is C_1 for h (\triangle) and \mathcal{H} (\circ) for \mathcal{V}_3 's solution for the smooth dam-break problem with $\alpha = 40m$	23
542 8	Numerical results of \mathcal{V}_3 at $t = 30s$ for the smooth dam-break problem with $\alpha = 2m$ for $\Delta x = 10/2^{10}m$ (—), $10/2^8m$ (—), $10/2^6m$ (—) and $10/2^4m$ (—).	24
544 9	On the left is L_1 for h (\triangle) and u (\square) and on the right is C_1 for h (\triangle), uh (\diamond) and \mathcal{H} (\circ) for \mathcal{V}_3 's solution for the smooth dam-break problem with $\alpha = 2m$	25
546 10	Numerical results of \mathcal{V}_3 at $t = 30s$ for the smooth dam-break problem with $\alpha = 0.4m$ for $\Delta x = 10/2^{10}m$ (—), $10/2^8m$ (—), $10/2^6m$ (—) and $10/2^4m$ (—).	26
548 11	On the left is L_1^* for h (\triangle) and u (\square) and on the right is C_1 for h (\triangle), uh (\diamond) and \mathcal{H} (\circ) for \mathcal{V}_3 's solution for the smooth dam-break problem with $\alpha = 0.4m$	27
550 12	Numerical results of \mathcal{V}_3 at $t = 30s$ for the smooth dam-break problem with $\alpha = 0.1m$ for $\Delta x = 10/2^{10}m$ (—), $10/2^8m$ (—), $10/2^6m$ (—) and $10/2^4m$ (—).	28
552 13	On the left is L_1^* for h (\triangle) and u (\square) and on the right is C_1 for h (\triangle), uh (\diamond) and \mathcal{H} (\circ) for \mathcal{V}_3 's solution for the smooth dam-break problem with $\alpha = 0.1m$	29
554 14	Numerical results for the smooth dam-break problem with $\alpha = 0.1m$ and $\Delta x = 10/2^{10}m$ for \mathcal{G} (—), \mathcal{E} (—), \mathcal{V}_3 (—) and \mathcal{V}_1 (—).	30
556 15	Numerical solution of smooth dam-break problem at $t = 300s$ by \mathcal{V}_3 with $\alpha = 0.1m$ for $\Delta x = 10/2^9m$ (—) and $10/2^8m$ (—).	31
558 16	Numerical solution of the smooth dam-break problem by \mathcal{V}_3 with $\alpha = 0.1m$ and $\Delta x = 10/2^9m$ at various times.	32
560 17	$h - h_2$ (—) and $u - u_2$ (—) for numerical solution of the smooth dam-break by \mathcal{V}_3 with $\alpha = 0.1m$ and $\Delta x = 10/2^9m$ at $t = 30s$ as in Figure 12.	33
562 18	$h - h_2$ (—) and $u - u_2$ (—) for numerical solution of the smooth dam-break by \mathcal{V}_3 with $\alpha = 0.1m$ and $\Delta x = 10/2^9m$ at $t = 300s$ as in Figure 15.	34
564 19	u_2 (—) and speed of the contact discontinuity (○) for numerical solutions of smoothed dam-break problems with different aspect ratios (h_1/h_0) by \mathcal{V}_3 where $\alpha = 0.1m$ and $\Delta x = 10/2^9m$ at $t = 100s$	35
566 20	Leading wave height plotted over time for the numerical solution of the smooth dam-break problem by \mathcal{V}_3 with $\alpha = 0.1m$ for $\Delta x = 10/2^9m$ (—) as in Figure 15.	36

- 569 21 Proportion of \mathcal{H} made up by horizontal kinetic energy (—), vertical kinetic energy
570 (—) and gravitational potential energy (—) for \mathcal{V}_3 's solution of the smooth dam-
571 break problem with $\alpha = 0.1m$ and $\Delta x = 10/2^9 m$ over time as in Figure 15. 37

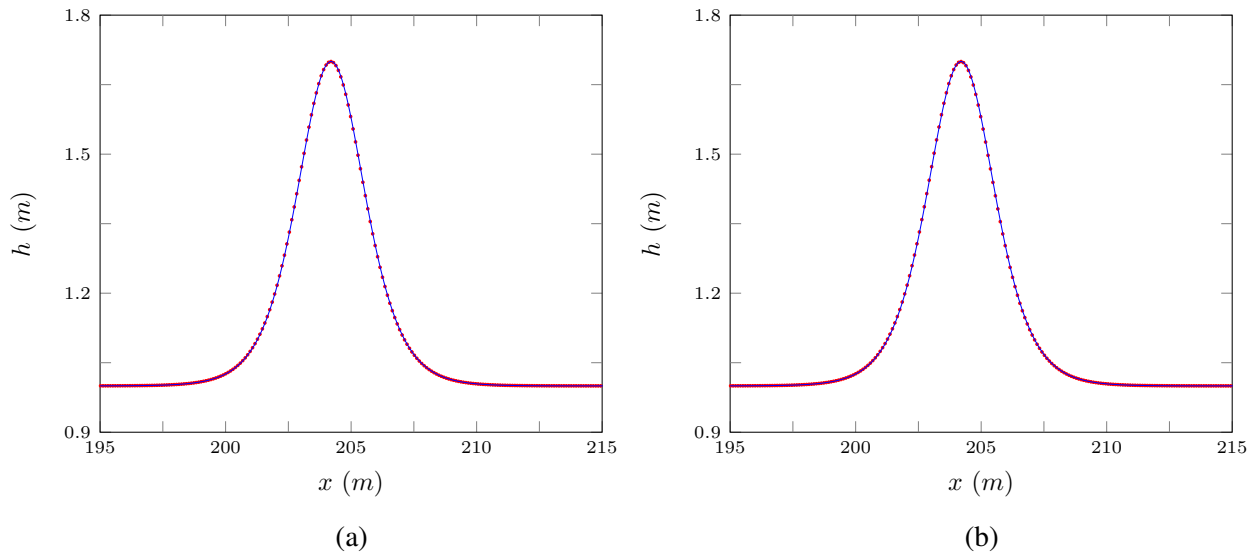
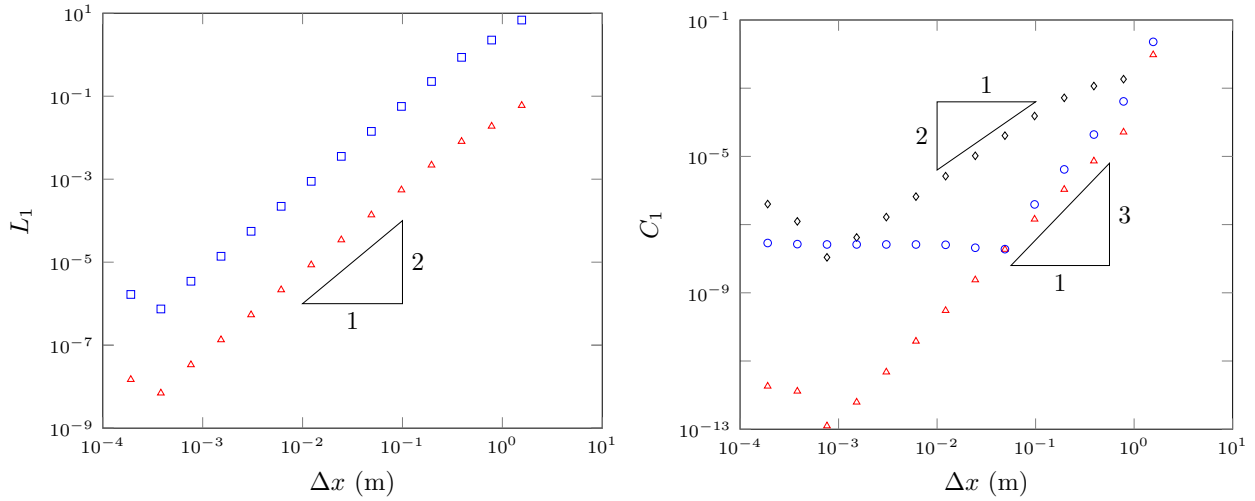
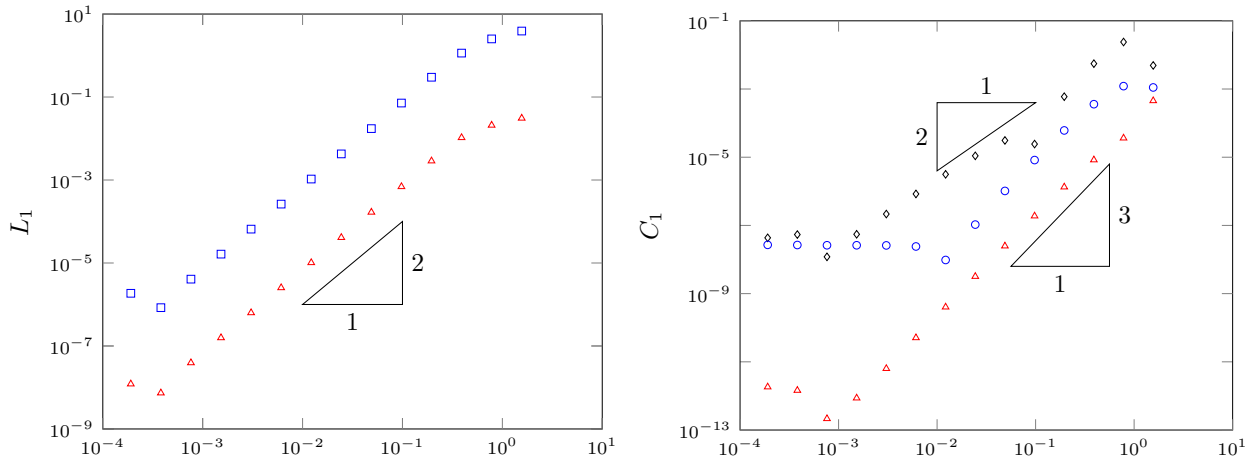


FIG. 1: Comparison between water profile of analytic solution (—) of the solitary wave problem (12) and numerical solution (●) with $\Delta x = 10/2^{12}m$ for \mathcal{G} (a) and \mathcal{E} (b) at $t = 50s$.



(a)



(b)

FIG. 2: On the left L_1 for h (\triangle) and u (\square) and on the right C_1 for h (\triangle), uh (\diamond) and \mathcal{H} (\circ) for the numerical solution of the solitary wave problem by \mathcal{G} (a) and \mathcal{E} (b).

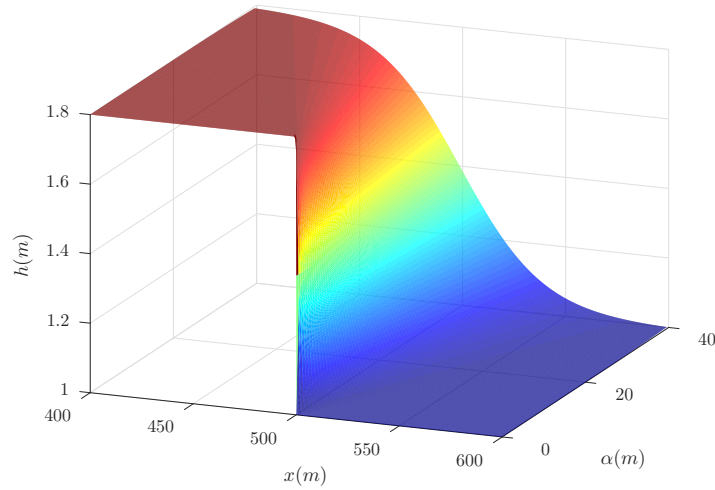


FIG. 3: Initial conditions for the smooth dam-break problem with $h_0 = 1m$, $h_1 = 1.8m$ and $x_0 = 500m$ as α varies.

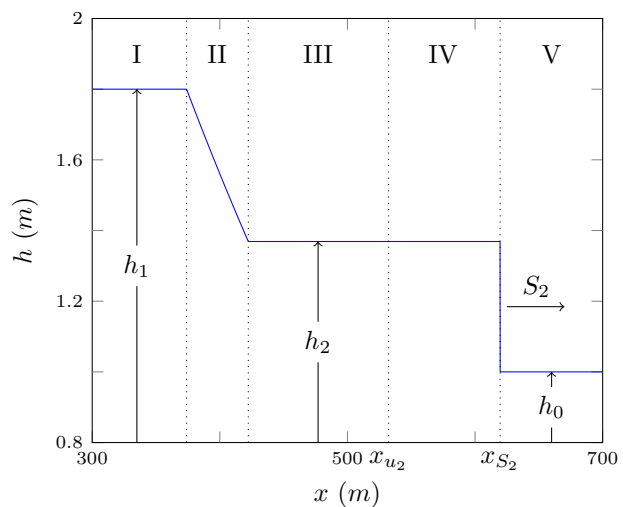


FIG. 4: Analytic solution at $t = 30s$ of the shallow water wave equations for the dam-break problem with $h_0 = 1m$, $h_1 = 1.8m$ and $x_0 = 100m$.

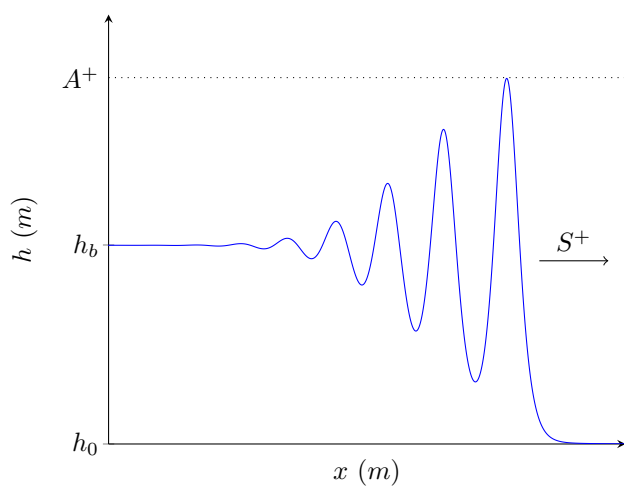


FIG. 5: Demonstration of quantities obtained by Whitham modulation for undular bores of the Serre equations.

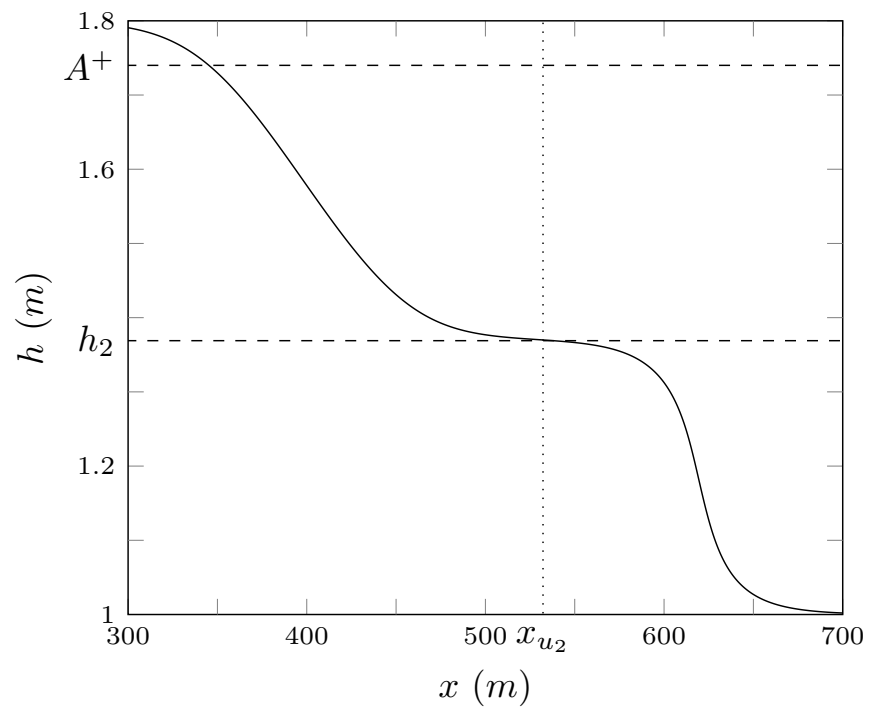


FIG. 6: Numerical results of \mathcal{V}_3 at $t = 30s$ for the smooth dam-break problem with $\alpha = 40m$ for $\Delta x = 10/2^4m$ (—).

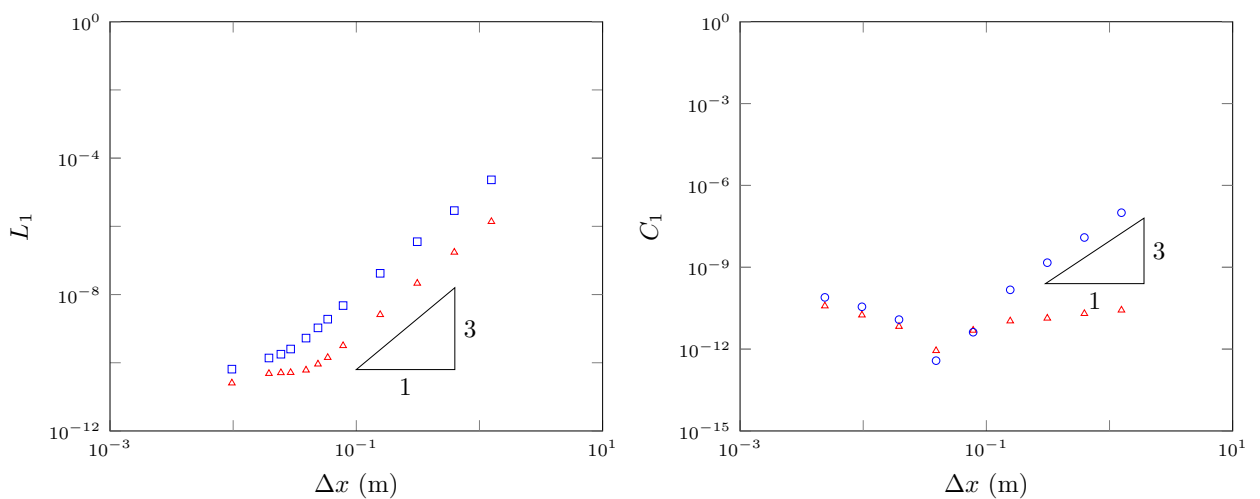


FIG. 7: On the left is L_1 for h (\triangle) and u (\square) and on the right is C_1 for h (\triangle) and \mathcal{H} (\circ) for \mathcal{V}_3 's solution for the smooth dam-break problem with $\alpha = 40m$.

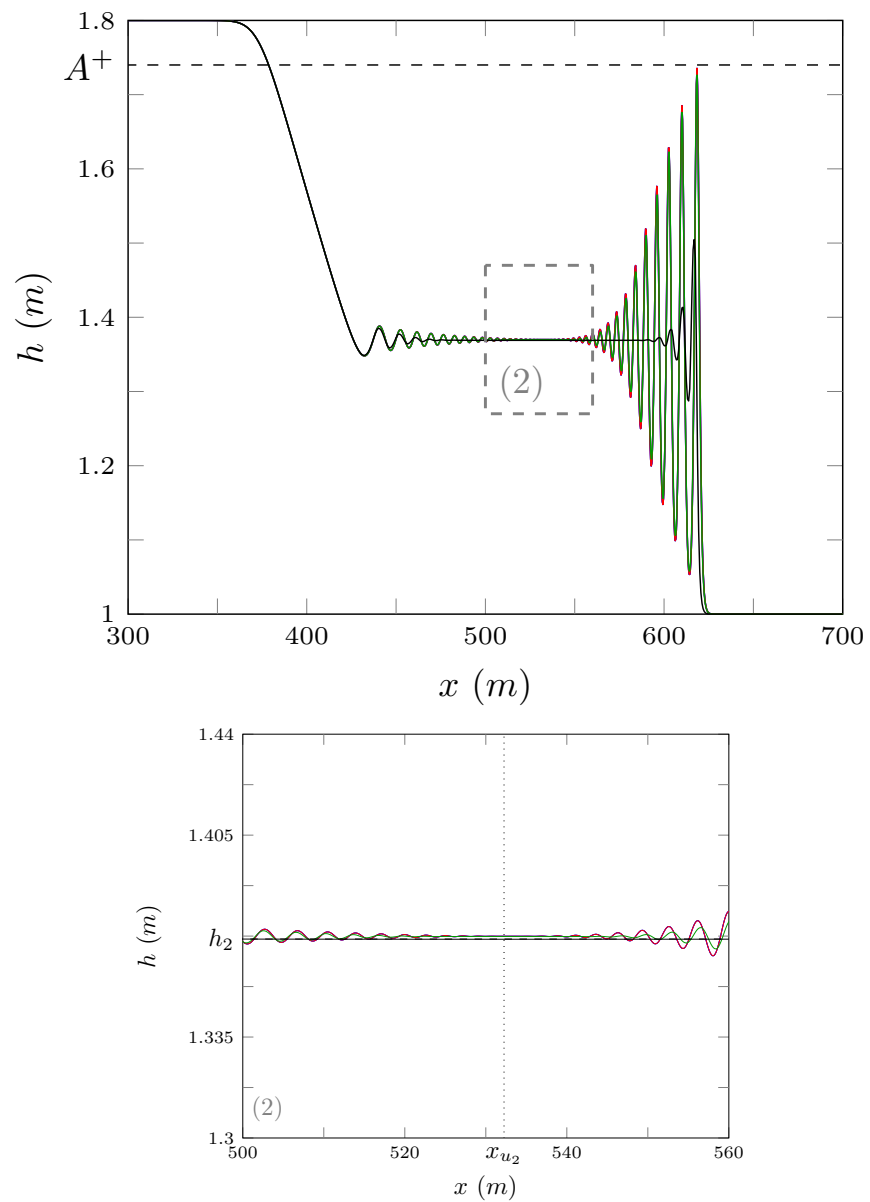


FIG. 8: Numerical results of \mathcal{V}_3 at $t = 30s$ for the smooth dam-break problem with $\alpha = 2m$ for $\Delta x = 10/2^{10}m$ (—), $10/2^8m$ (—), $10/2^6m$ (—) and $10/2^4m$ (—).

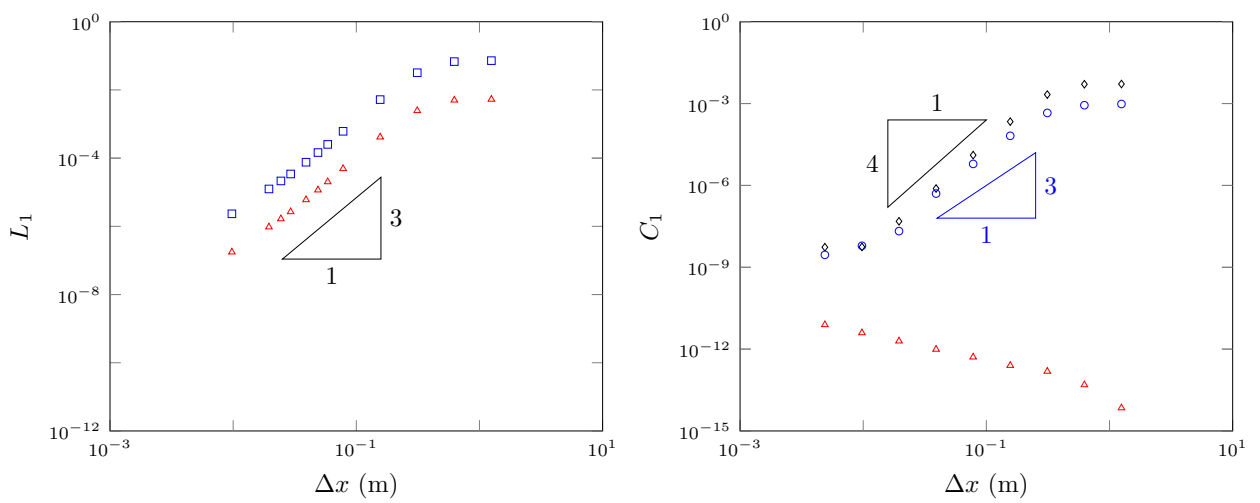


FIG. 9: On the left is L_1 for h (\triangle) and u (\square) and on the right is C_1 for h (\triangle), uh (\diamond) and \mathcal{H} (\circ) for \mathcal{V}_3 's solution for the smooth dam-break problem with $\alpha = 2m$.

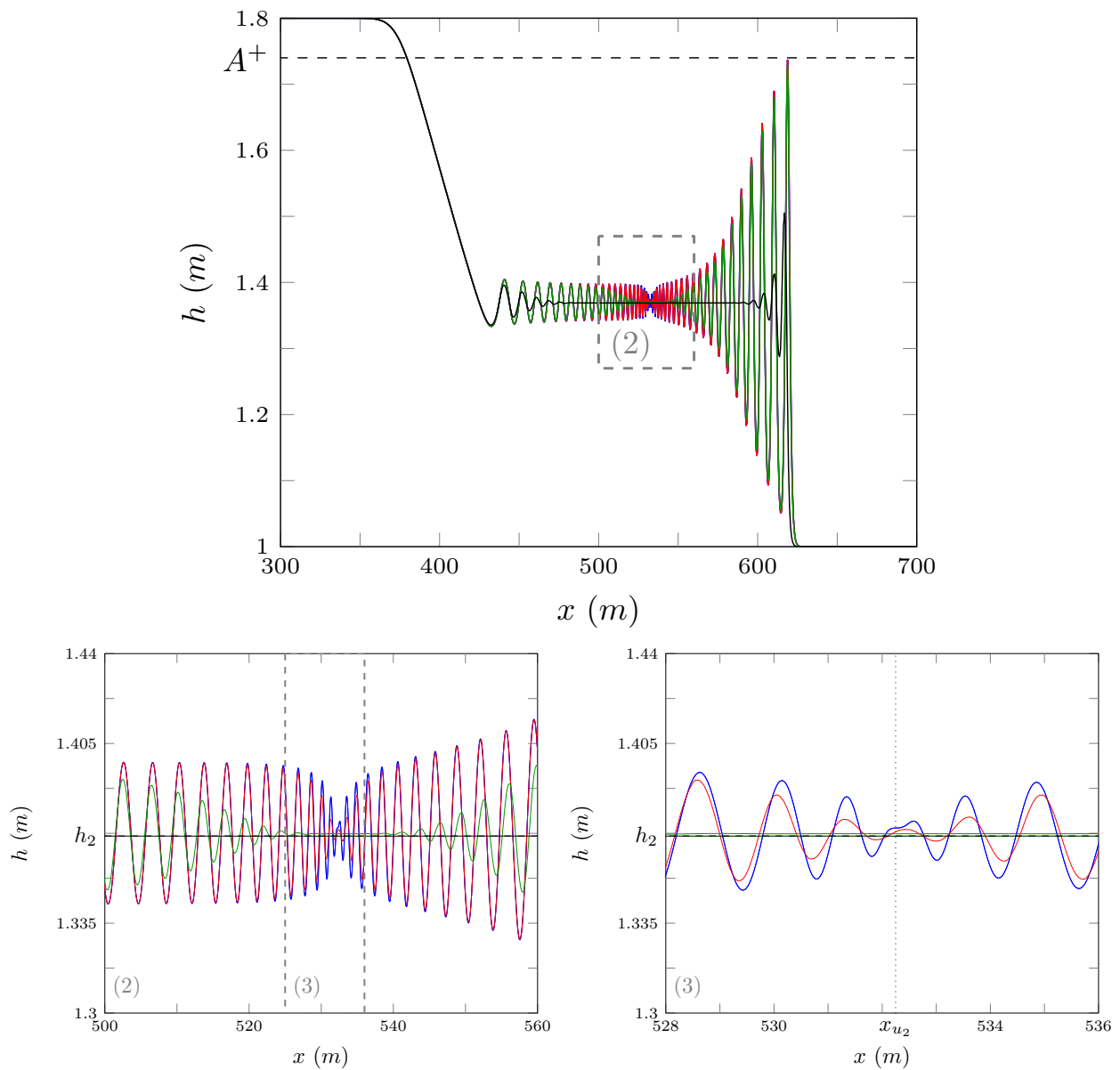


FIG. 10: Numerical results of \mathcal{V}_3 at $t = 30s$ for the smooth dam-break problem with $\alpha = 0.4m$ for $\Delta x = 10/2^{10}m$ (—), $10/2^8m$ (—), $10/2^6m$ (—) and $10/2^4m$ (—).

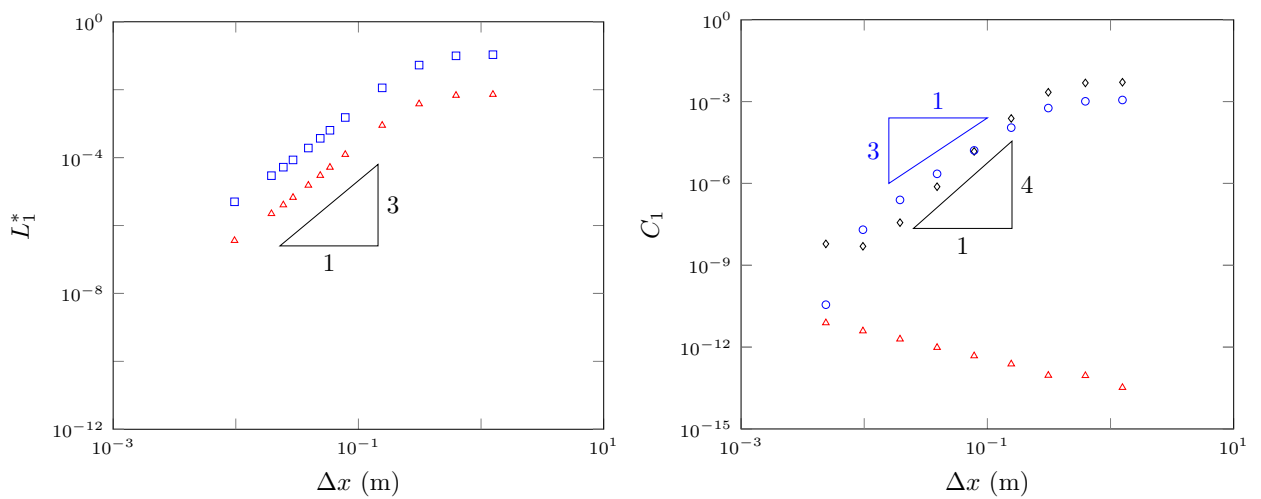


FIG. 11: On the left is L_1^* for h (\triangle) and u (\square) and on the right is C_1 for h (\triangle), uh (\diamond) and H (\circ) for \mathcal{V}_3 's solution for the smooth dam-break problem with $\alpha = 0.4\text{m}$.

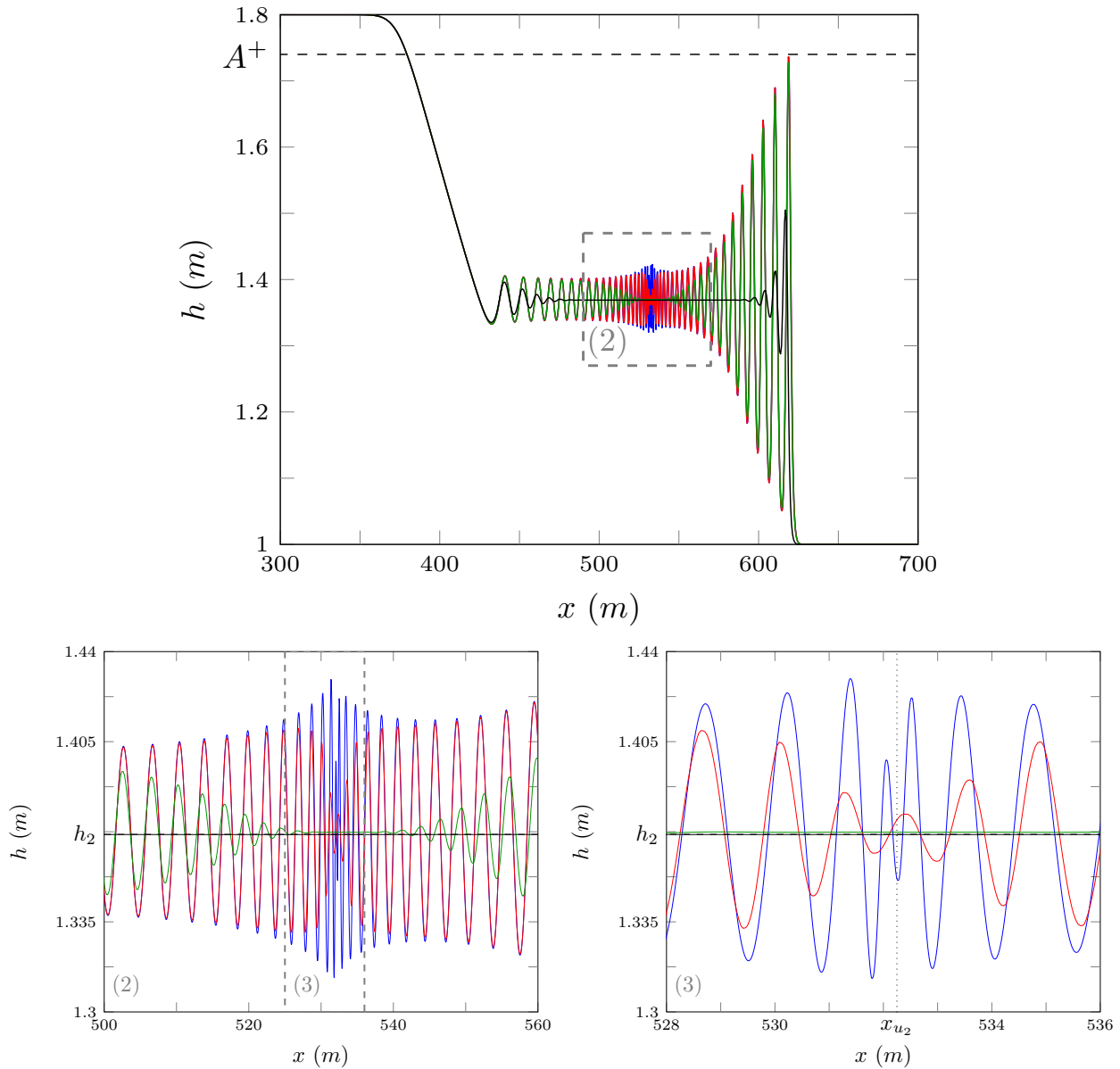


FIG. 12: Numerical results of \mathcal{V}_3 at $t = 30s$ for the smooth dam-break problem with $\alpha = 0.1m$ for $\Delta x = 10/2^{10}m$ (—), $10/2^8m$ (—), $10/2^6m$ (—) and $10/2^4m$ (—).

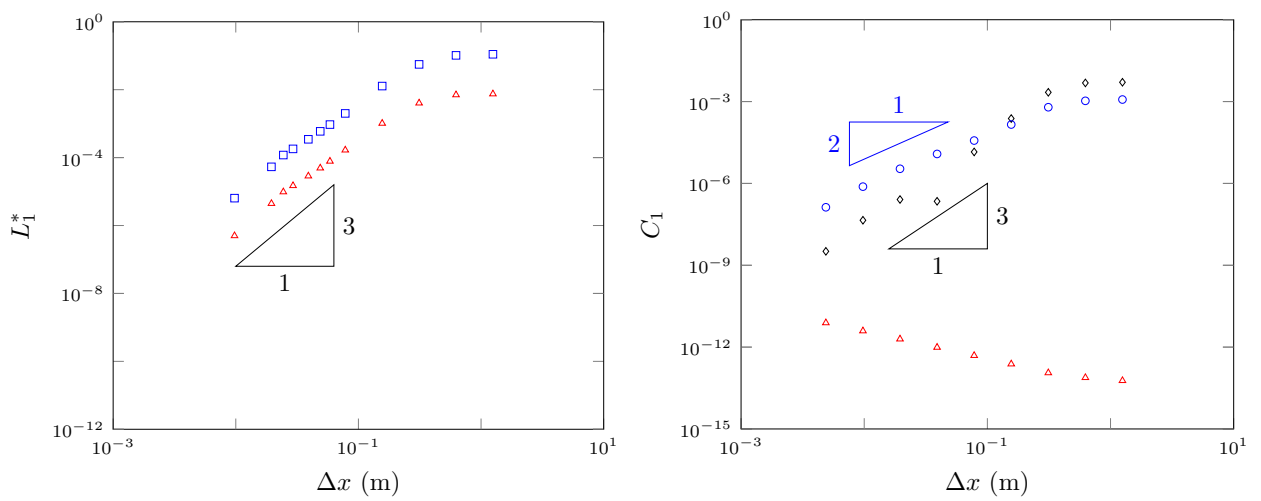


FIG. 13: On the left is L_1^* for h (\triangle) and u (\square) and on the right is C_1 for h (\triangle), uh (\diamond) and \mathcal{H} (\circ) for \mathcal{V}_3 's solution for the smooth dam-break problem with $\alpha = 0.1m$.

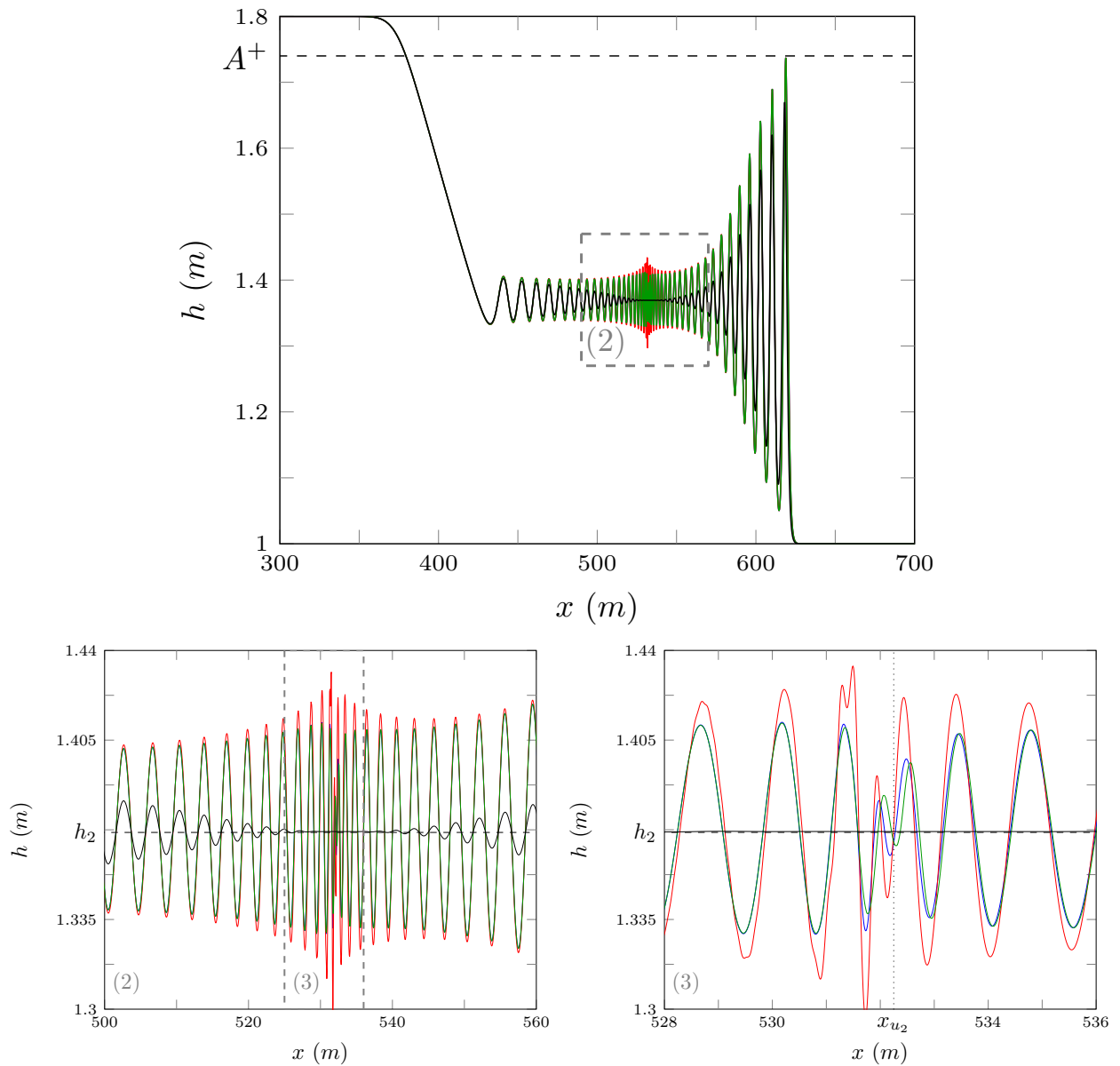


FIG. 14: Numerical results for the smooth dam-break problem with $\alpha = 0.1m$ and $\Delta x = 10/2^{10}m$ for \mathcal{G} (—), \mathcal{E} (—), \mathcal{V}_3 (—) and \mathcal{V}_1 (—).

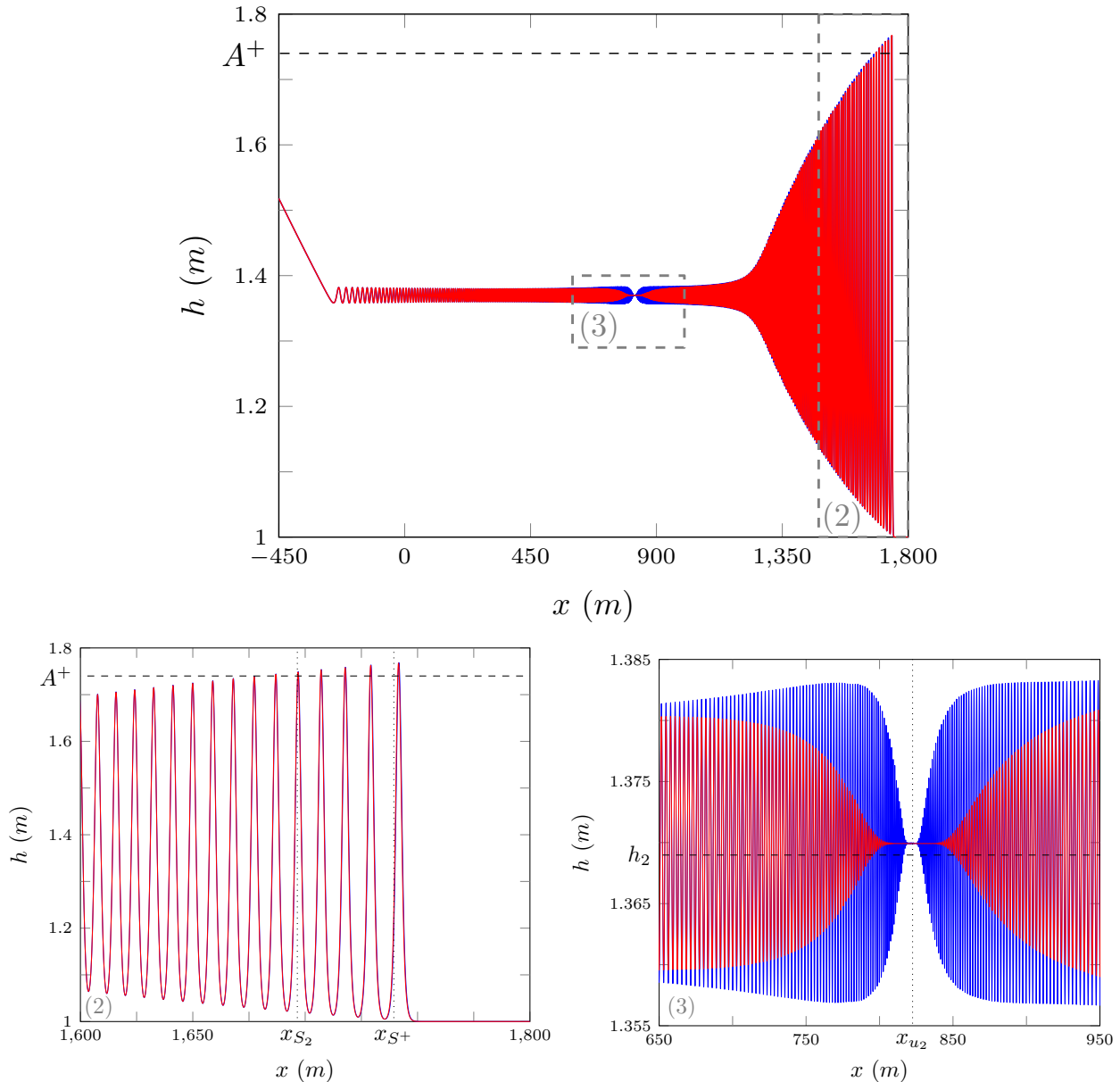


FIG. 15: Numerical solution of smooth dam-break problem at $t = 300s$ by \mathcal{V}_3 with $\alpha = 0.1m$ for $\Delta x = 10/2^9 m$ (—) and $10/2^8 m$ (—).

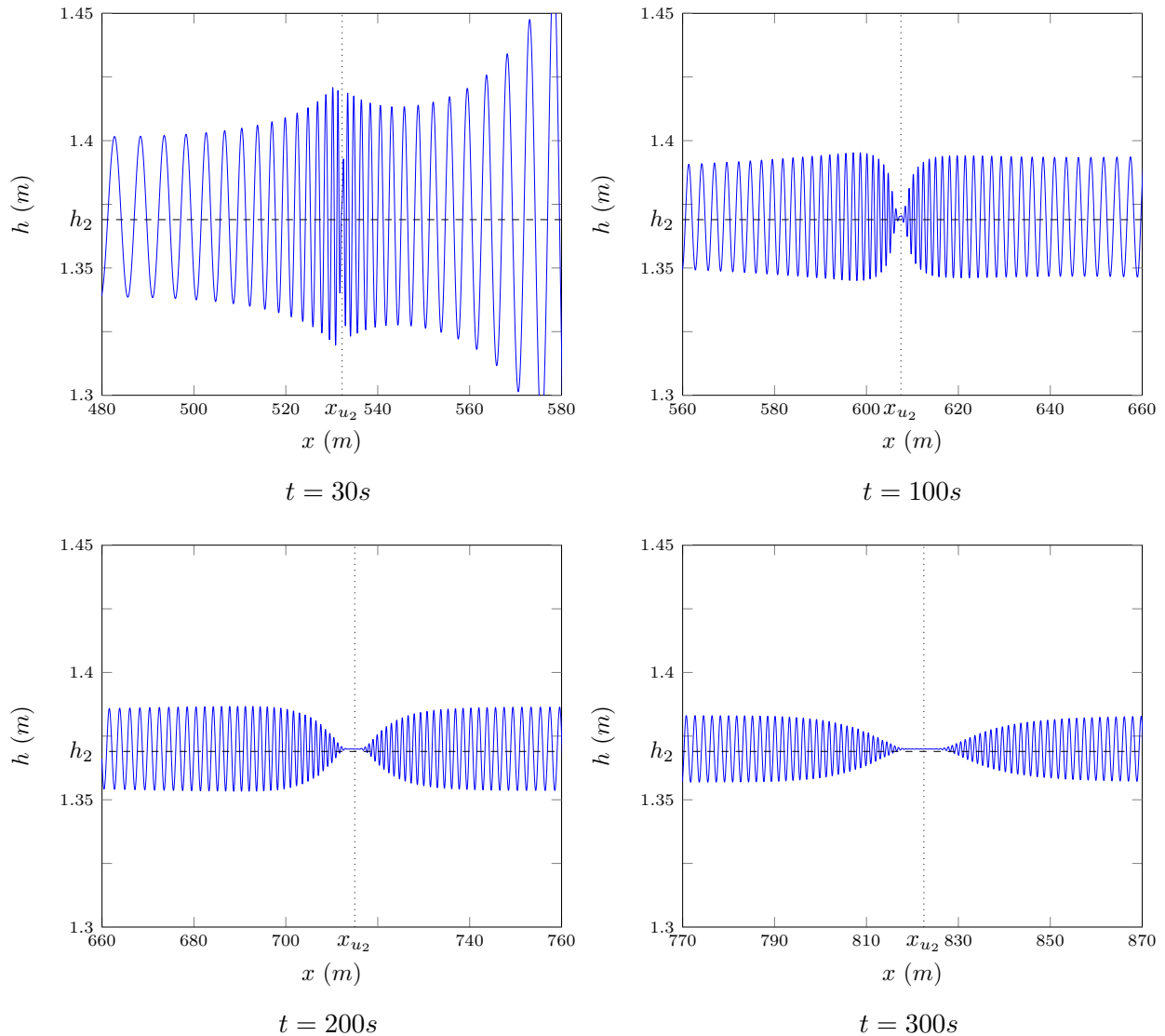


FIG. 16: Numerical solution of the smooth dam-break problem by \mathcal{V}_3 with $\alpha = 0.1m$ and $\Delta x = 10/2^9 m$ at various times.

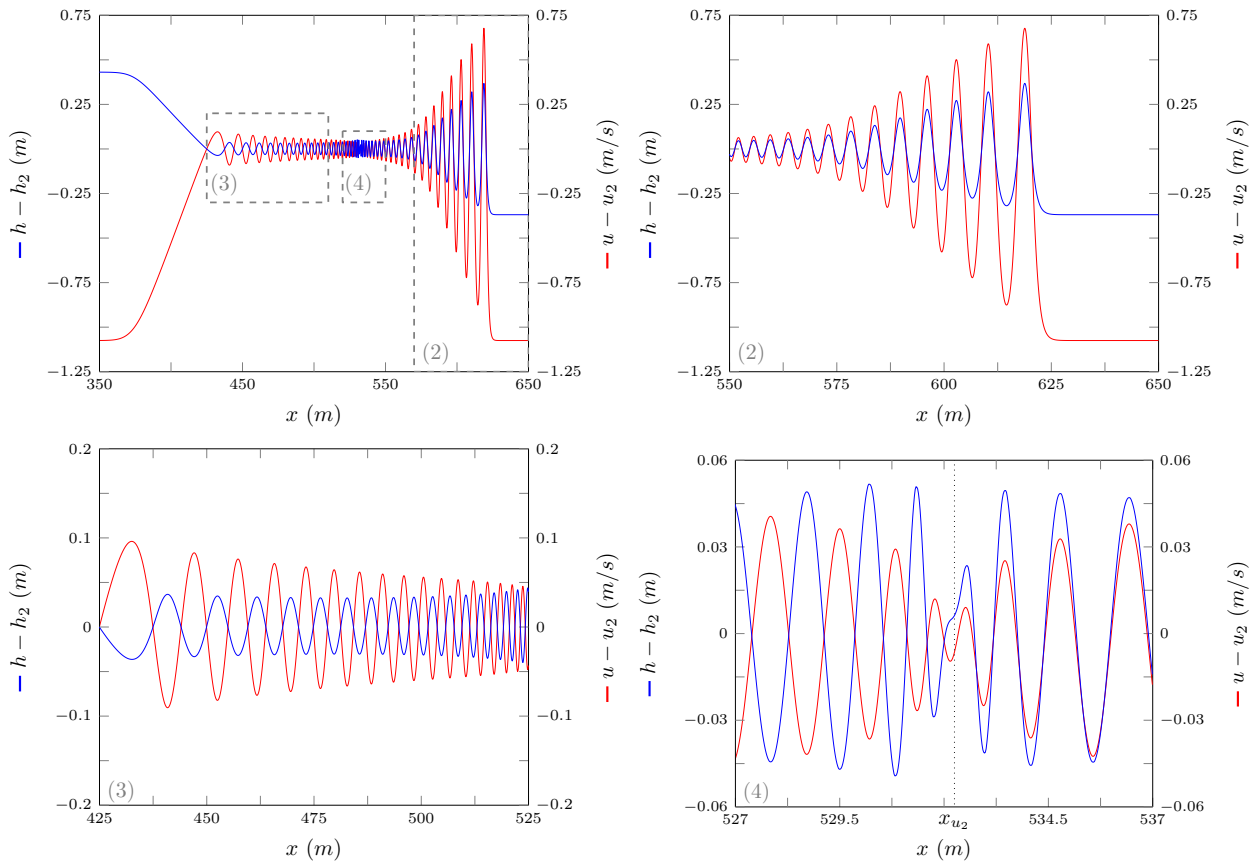


FIG. 17: $h - h_2$ (—) and $u - u_2$ (—) for numerical solution of the smooth dam-break by \mathcal{V}_3 with $\alpha = 0.1m$ and $\Delta x = 10/2^9 m$ at $t = 30s$ as in Figure 12.

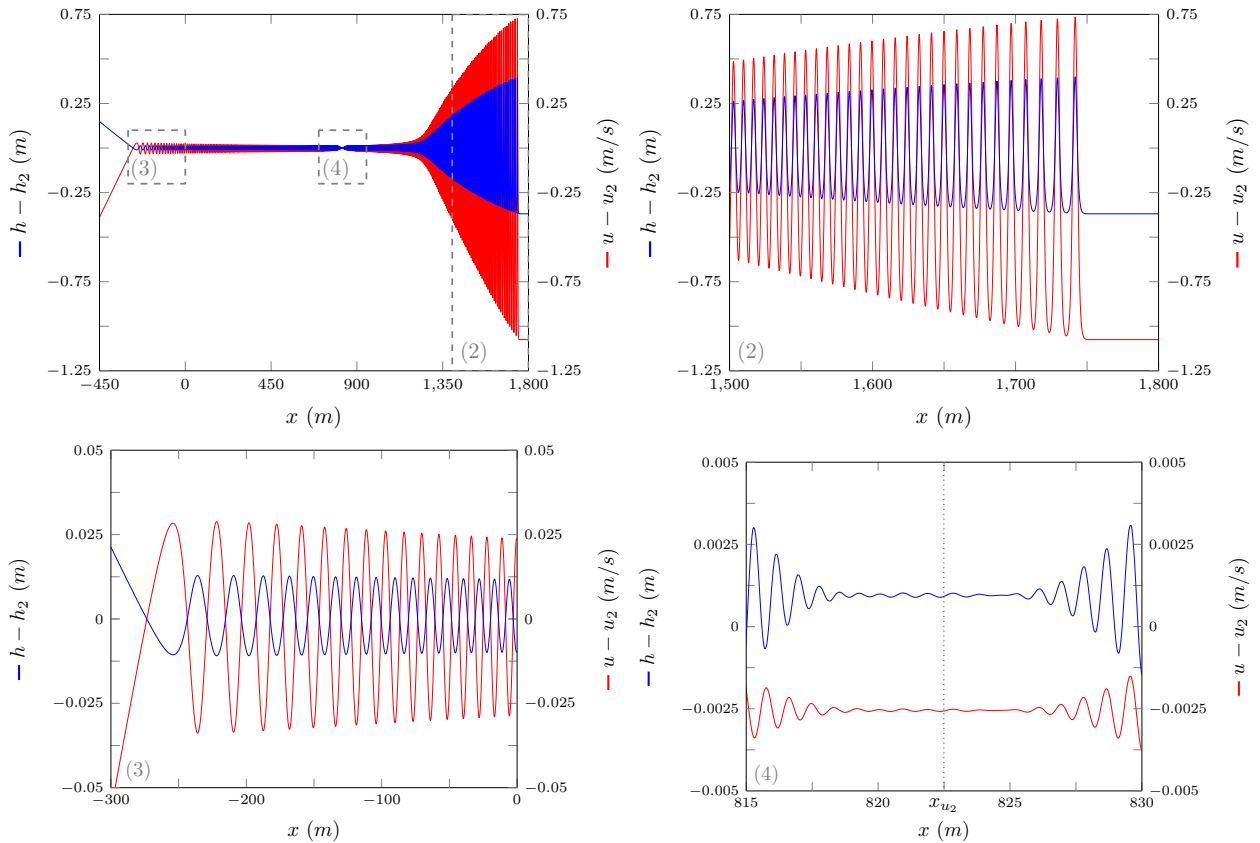


FIG. 18: $h - h_2$ (—) and $u - u_2$ (—) for numerical solution of the smooth dam-break by \mathcal{V}_3 with $\alpha = 0.1m$ and $\Delta x = 10/2^9 m$ at $t = 300s$ as in Figure 15.

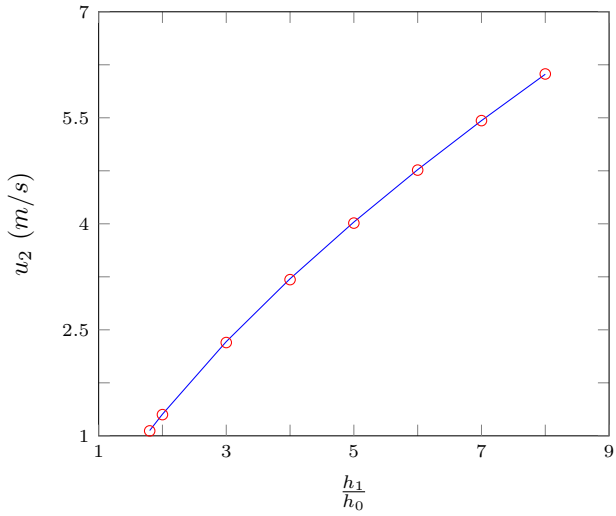


FIG. 19: u_2 (—) and speed of the contact discontinuity (○) for numerical solutions of smoothed dam-break problems with different aspect ratios (h_1/h_0) by \mathcal{V}_3 where $\alpha = 0.1m$ and $\Delta x = 10/2^9 m$ at $t = 100s$.

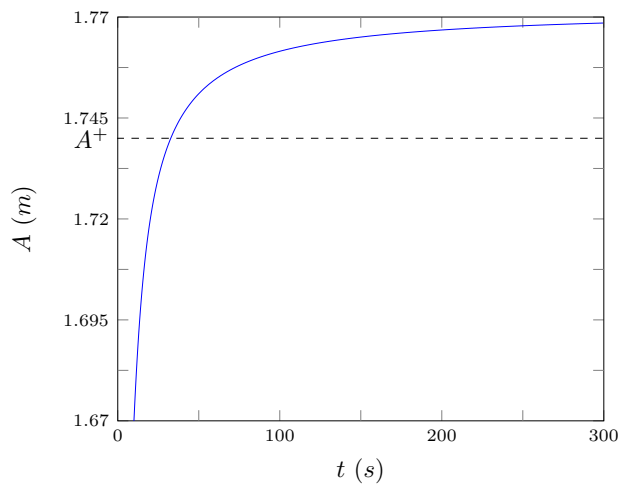


FIG. 20: Leading wave height plotted over time for the numerical solution of the smooth dam-break problem by \mathcal{V}_3 with $\alpha = 0.1m$ for $\Delta x = 10/2^9 m$ (—) as in Figure 15.

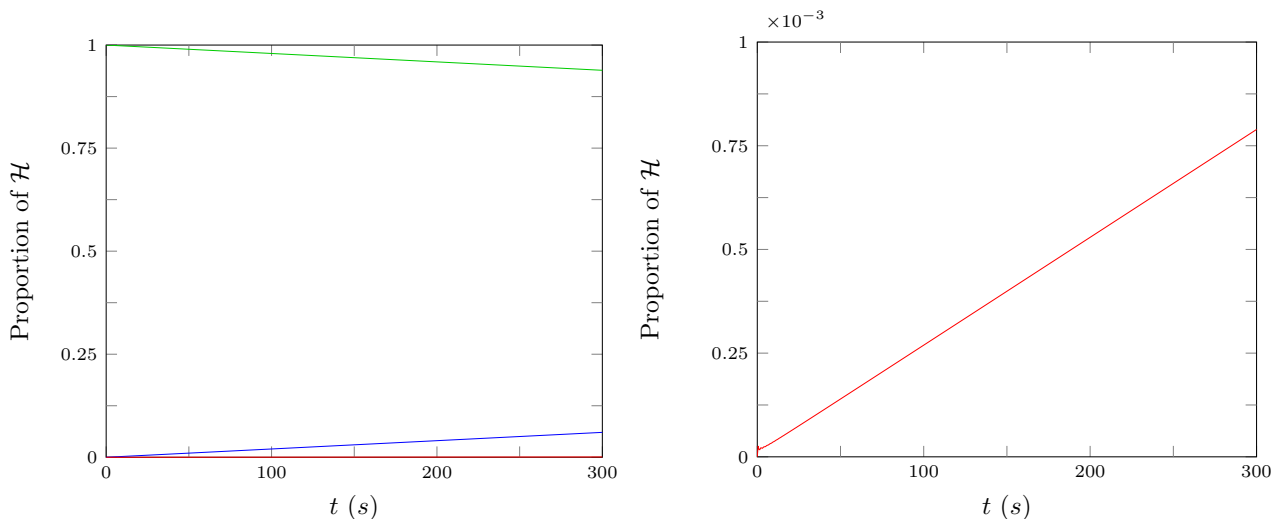


FIG. 21: Proportion of \mathcal{H} made up by horizontal kinetic energy (—), vertical kinetic energy (—) and gravitational potential energy (—) for \mathcal{V}_3 's solution of the smooth dam-break problem with $\alpha = 0.1m$ and $\Delta x = 10/2^9 m$ over time as in Figure 15.